Enhancing Micro Free Flow Electrophoresis: Detection, Application, and Fabrication

A Dissertation

SUMBITTED TO THE FACULTY OF THE

UNIVERSITY OF MINNESOTA

BY

Matthew B. LeMon

IN PARTIAL FULLFILMENT OF THE REQUIREMENTS

FOR THE DEGREE OF

DOCTOR OF PHILOSOPHY

Michael T. Bowser, Advisor

April 2023

Acknowledgments

My chemistry journey began in the IB program at Champlin Park High School in Brooklyn Park, MN, where I quickly found I had a natural affinity for the subject. My chemistry teacher, Beth Bethkey, played a major role in my decision to pursue chemistry further. Her rampant enthusiasm for the subject, fun loving attitude, and insightful demonstrations created an environment that helped me thrive and sparked my desire to learn more about the field. I started undergrad at The College of St. Scholastica in Duluth, MN the Fall after graduating pursuing a double major in Chemistry and Biochemistry. There under the tutelage of Dr. Bret Johnson, Dr. Jennifer Maki, Dr. Lawrence McGahey, Dr. Timothy Trygstad, Dr. Allen Chaparadza, and Dr. Paul Stein my desire for understanding continued to grow and pushed me to pursue my Ph.D. in Chemistry.

I would like to thank Dr. Lawrence McGahey and my undergraduate advisor Dr. Paul Stein for having me as research assistants over multiple summers. Through their contributions, a pragmatic approach to chemistry valuing empirical results over theoretical possibilities was instilled in me that I am grateful for every day. I would like to extend further thanks to Dr. Stein, under whom I attained authorship on my first scientific paper with my fellow undergrad James McClusky.

I would also like to thank my Ph.D. advisor, Dr. Mike Bowser. You have been instrumental in my development, granting me the freedom to explore what interested me most while providing direction whenever I needed it. I am eternally grateful for your seemingly unending kindness and how you kept me driving forward whenever I lost motivation. To my fellow Bowser Group members, Dr. Matt Geiger, Dr. Rachel Harstad, Dr. Kailey Soller, Dr. Megan Weisenberger, Dr. Sarah Anciaux, Dr. Alexander Johnson,

Dr. Sean Dembowski, Dr. Nic Brinza, Dr. Sarah Nelson, Cecilia Douma, and Gretchen Burke, thank you for making my time in this group wonderful. Thank you for the enlightening and entertaining conversations in the lab and over lunch, and most of all, thank you for tolerating my coarseness and helping me become a more refined person.

Thank you to the Minnesota Nano Center for the use of their cleanroom facilities which were crucial to my research. Thank you to the Earl E. Bakken Medical Device Center for their service producing poly-jet 3D prints for my research. A special thank you to Dr. David Wood and his lab for providing the thermal press that made much of my work possible.

Finally, to my parents, I would never have gotten where I am today without you. You instilled a thirst for knowledge in me from a young age and pushed me to constantly improve. You gave me the freedom to pave my own path in life while always being there to support me whenever I needed it. You build me up whenever I am down and keep me grounded whenever I get ahead of myself. I don't say it often enough, but I am grateful for your role in shaping me into the man I am today, and I love you both wholeheartedly.

Abstract

Micro Free Flow Electrophoresis (μFFE) is a separation technique where analytes are moved through a planar separation channel via pressure driven flow. Analytes streams are deflected laterally within an electric field applied perpendicular to the flow and separated from one another based on differences in their electrophoretic mobility. Notably, μFFE is capable of continuously separating analytes making it uniquely useful for a range of applications such as multidimensional separations, microscale sample purification, and continuous on-line monitoring. This work focuses on improving the sensitivity of laser induced fluorescence (LIF) detection via modifying the laser alignment, exploring new device designs for rapid on-line buffer exchange, and developing a novel fabrication technique for hot embossing μFFE devices in cyclic olefin copolymer (COC) with the goal of expanding μFFE's use in analytical workflows. A new laser alignment for LIF was explored, focusing the laser light through the side of the device instead of spreading it into a line and reflecting it down onto it. Improvement in the limit of detection (LOD) for fluorescein was obtained in a glass μFFE device using this alignment; however, it was found to be incompatible with 3D printed acrylonitrile butadiene styrene (ABS) due to excessive scattering of the laser light. New μFFE device designs were developed and modeled using Multiphysics modeling software to optimize a design for rapid on-line buffer exchange. This was performed with the intent of interfacing incompatible separation modes with electrospray ionization mass spectrometry (ESI-MS) to develop novel multi-attribute analysis techniques for the assessment of therapeutic monoclonal antibodies (mAbs). Lastly, a novel fabrication technique for μFFE was developed to hot emboss μFFE devices in COC utilizing a poly jet 3D printed master mold. The performance of devices produced this way were tested

via a separation of three fluorescent dyes. Their LODs quantified and compared to similar ABS and glass µFFE devices.

Table of Contents

List of Figures

List of Tables

List of Abbreviations

2D	Two-Dimensional
µFFE	Micro Free Flow Electrophoresis
ABS	Acrylonitrile Butadiene Styrene
AC	Affinity Chromatography
ACE	Affinity Capillary Electrophoresis
CAD	Computer-aided Design
CE	Capillary Electrophoresis
cIEF	Capillary Isoelectric Focusing
COC	Cyclic Olefin Copolymer
COP	Cyclic Olefin Polymer
DMSO	Dimethyl Sulfoxide
DRIE	Deep Reactive Ion Etching
EOF	Electroosmotic Flow
EFL	Effective Focal Length
ESI	Electrospray Ionization
ESI-MS	Electrospray Ionization Mass Spectrometry
FDM	Fused Deposition Modeling
FFE	Free Flow Electrophoresis
GC	Gas Chromatography
GC×GC	Two Dimensional Gas Chromatography
HEPES	4-(2-Hydroxyethyl)-1-Piperazineethanesulfonic Acid
HP-β-CD	Hydroxypropyl-β-Cyclodextrin
IAC	Ion Affinity Chromatography
IEF	Isoelectric Focusing

ITP	Isotachophoresis
LC	Liquid Chromatography Coupled to Micro Free Flow Electrophoresis
LC×µFFE	Liquid Chromatography
LC×LC	Two Dimensional Liquid Chromatography
LIF	Laser Induced Fluorescence
LOD	Limit of Detection
mAb	Monoclonal Antibody
MEKC	Micellar Electrokinetic Chromatography
MS	Mass Spectrometry
nLC	Nano Liquid Chromatography
nLC×µFFE	Nano Liquid Chromatography Coupled to Micro Free Flow Electrophoresis
PC	Poly Carbonate
PDMS	Polydimethylsiloxane
PEA	Phosphorylethanolamine
PLA	Polylactic Acid
PMMA	Polymethyl Methacrylate
PTFE	Polytetrafluoroethylene
RP-HPLC	Reversed Phase High Performance Liquid Chromatography
SEC	Size Exclusion Chromatography
SELEX	Selective Evolution of Ligand by Exponential Enrichment
SERS	Surface Enhanced Raman Spectroscopy
SLA	Stereolithography
ZE	Zone Electrophoresis

Chapter 1
Introduction

Micro Free-Flow Electrophoresis Separation Theory

Micro Free Flow Electrophoresis (μFFE) is an analytical separation technique first developed by Raymond et. al.[1] μFFE is based on miniaturizing Free Flow Electrophoresis (FFE), a technique that separates analytes in space based on differences in electrophoretic mobility[1]. In μFFE, sample is introduced into a narrow rectangular channel and driven down the channel by pressure driven buffer flow. Voltage is applied to electrodes on both sides of the channel, generating an electric field perpendicular to the pressure driven flow. The electric field deflects analytes laterally within the channel, which separates them into discrete streams based on their charge and size. The distance each analyte is deflected is given by the equation[1,2]:

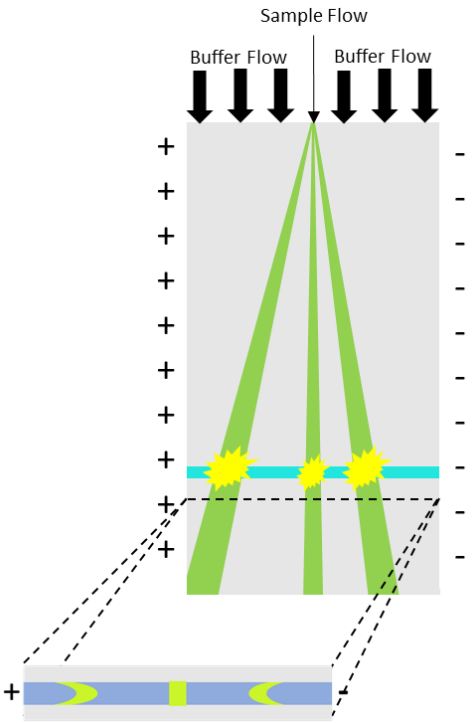

Figure 1.1 A schematic of a μFFE device separating three fluorescent analytes. The cross-section showcases the effect of hydrodynamic broadening on the analyte stream shape.

$$d = Et\left(\mu_{ep} + \mu_{eo}\right) = \frac{EL\mu_{total}}{v} \tag{1.1}$$

where d is the deflection distance, E is the electric field strength, t is the time the analyte has spent in the electric field, μ_{ep} is the analyte electrophoretic mobility, μ_{eo} is the electroosmotic mobility, μ_{total} is the combined mobilities, L is the length separation channel prior to detection, and v is the linear velocity of the buffer flow down the channel. The product Et is referred to as the separating power of a μFFE separation[2].

μFFE, like capillary electrophoresis (CE), can be run in a variety of different separating modes such as zone electrophoresis (ZE)[1,3–10], isoelectric focusing (IEF)[11–18], and isotachophoresis (ITP)[19–21]. Furthermore, μFFE has been shown to be an effective means of separating a wide array of analytes such as fluorescent dyes[2,4–6], proteins[6,22], and amino acids.[23] Its major strength is the ability to perform continuous separation of analytes without the need for discrete plugs of sample. Due to this ability to continuously inject, separate, and detect analytes, μFFE has unique advantages for applications such as microscale sample purification[24,25], aptamer selection[9], online buffer exchange[13], and online reaction monitoring.[25,26] The continuous nature of μFFE also makes it a powerful tool for two dimensional (2D) separations[23,27–30], particularly as the second dimension.

Sample Broadening in μFFE

The factors contributing to broadening in μFFE separations have been well explored and modeled in literature.[2,7,31] The overall peak variance (σ^2_{total}) can be caused by the contributions of injection stream width (σ^2_{inj}), analyte diffusion (σ^2_{D}), electrodynamic broadening (σ^2_{ED}), hydrodynamic broadening (σ^2_{HD}), and electrohydrodynamic broadening (σ^2_{EHD}). Taken together a general broadening equation for μFFE separations can be generated.

$$\sigma^2_{total} = \sigma^2_{inj} + \sigma^2_{D} + \sigma^2_{ED} + \sigma^2_{HD} + \sigma^2_{EHD} \quad (1.2)$$

Electrodynamic broadening is a phenomenon that occurs due to electroosmotic flow (EOF) within closed device designs. Closed device designs feature electrodes that are physically separated from the separation channel. The physical barriers prevent fluid movement caused by EOF from exiting the separation channel which causes it to recirculate within the separation channel. The recirculation results in a pressure driven

flow perpendicular to the bulk fluid movement in the device, causing analyte stream broadening due to its parabolic profile.[2,32] The device designs discussed herein utilize open designs, featuring no barriers between the electrodes and separation channel, thus electrodynamic broadening can be ignored.

Electrohydrodynamic broadening occurs due to a difference in the conductivity of the sample stream and the buffer driving flow in the device.[33] The difference in conductivity results in higher or lower electric field strength within the sample stream, which causes analytes to migrate faster or slower within the sample stream. Specifically, broadening occurs when the conductivity of the sample stream is higher than the buffer, wherein analytes will begin migrating faster once leaving the sample stream. Conversely, when the conductivity of the sample stream is lower the analytes will migrate slower when leaving the sample stream resulting in narrower peaks. The separations discussed here will have well matched buffer and sample stream conductivity, and thus electrohydrodynamic broadening can be ignored. With electrodynamic and electrohydrodynamic factors removed, the general equation for stream broadening in an open channel µFFE device can be condensed to:

$$\sigma_{total}^2 = \sigma_{inj}^2 + \sigma_D^2 + \sigma_{HD}^2 \quad (1.3)$$

The variance caused by injection width is a common factor in separations. In µFFE injection width is determined by the width of the sample stream as it enters the device (w_{inj}), and is defined by the equation [2]:

$$\sigma_{inj}^2 = \frac{w_{inj}^2}{12} \quad (1.4)$$

Variance caused by diffusion is also a common factor in separations and is given by the equation:

$$\sigma_D^2 = 2Dt = \frac{2DL}{v} \quad (1.5)$$

Where D is the diffusion coefficient of the analyte, and t is the residence time of the analyte within the device. In µFFE, the residence time in the device is determined by the length of the separation channel prior to detection (L), and the linear velocity of buffer flow in the channel (v).[2]

The variance due to hydrodynamic broadening is a result of the interaction between the pressure driven flow down the device and the electric field perpendicular to it. The parabolic nature of pressure driven flow causes analytes near the top and bottom of the separation channel to move slower through the device. Consequently, these analytes experience the electric field longer than the analytes moving down the center of the channel. The extra residence time in the electric field causes these analytes to be deflected further, resulting in the crescent stream shape shown in Figure 1.1. Hydrodynamic broadening is given by the equation:

$$\sigma_{HD}^2 = \frac{h^2 d^2 v}{105DL} \quad (1.6)$$

Where h is the channel height, d is the deflection distance, v is the linear velocity of the buffer, D is the diffusion coefficient of the analyte, and L is the length of the separation channel prior to detection.[2] Utilizing equations 1.4, 1.5, and 1.6 equation 1.3 can be rewritten as:

$$\sigma_{total}^2 = \frac{w_{inj}^2}{12} + \frac{2DL}{v} + \frac{h^2 d^2 v}{105DL} \quad (1.7)$$

Where w_{inj} is the injection width, D is the diffusion coefficient of the analyte, L is the length of the separation channel prior to detection, v is the linear buffer velocity, h is the channel height, and d is the deflection distance.[2]

Notably, joule heating is not a factor in μFFE separations as the high surface area to volume ratio quickly dissipates heat generated during separation, and the applied voltage is limited due to electrolysis products that form at the electrodes. If joule heating occurred in a μFFE device it is unlikely it would result in increased stream broadening. In a μFFE device joule heating results in a temperature gradient across the separation channel with the highest temperatures at its center. The higher temperature lowers the viscosity of the fluid, which increases the electrophoretic mobility of the analytes and thus how far they are deflected. However, the lower fluid viscosity also increases the flow rate down the channel, reducing analyte residence time within the device and thus causing little to no net change in stream position. Furthermore, while the increased temperature results in more diffusive broadening, it also results in faster equilibration along the height of the channel reducing the effects of hydrodynamic broadening.

As shown by Fonslow and Bowser[2], equation 1.7, which predicts band width, and 1.1, which predicts stream location, can be combined to predict the resolution (R_s) of a separation at any linear buffer velocity with any electric field strength:

$$R_s = \frac{d_1 - d_2}{(w_1 + w_2)/2} = \frac{(\mu_{total,1} - \mu_{total,2})Et}{2\left(\sqrt{\frac{w_{inj}^2}{12} + \frac{2D_1L}{v} + \frac{h^2 d_1^2 v}{105 D_1 L}} + \sqrt{\frac{w_{inj}^2}{12} + \frac{2D_2L}{v} + \frac{h^2 d_2^2 v}{105 D_2 L}}\right)} \quad (1.8)$$

From equation 1.8 Fonslow and Bowser noted several useful trends can be observed depending on the dominant source of broadening.[2]

In cases where injection width is the dominant source of broadening equation 1.8 becomes [2]:

$$R_s = \frac{\sqrt{0.75}\Delta\mu E t}{w_{inj}^2} \tag{1.9}$$

Where Δμ is the difference in the total mobility of the analytes. Equation 1.9 shows that under such conditions the resolution of the analytes increases linearly with separating power (Et). However, it is atypical for injection width the be the dominant source of broadening in μFFE separations.

Under conditions where the linear flow velocity in the device is very low, diffusion becomes the dominant source of broadening and equation 1.8 can be approximated by the equation [2]:

$$R_s \approx \Delta\mu E\sqrt{\frac{L}{32D\nu}} \tag{1.10}$$

Equation 1.10 shows that when diffusion is the dominant source of broadening, resolution scales linearly with the electric field strength (E), while scaling inversely with the square root of the linear velocity (v). Diffusion is commonly the dominant source of broadening for streams that experience little deflection.

Under typical μFFE operating conditions, hydrodynamic broadening is the dominant source of broadening in a separation, which occurs when the liner velocity of flow and deflection distance of analytes are high. Under these conditions equation 1.8 is approximated by [2]:

$$R_s \approx \frac{\Delta\mu}{4h\mu}\sqrt{\frac{105L}{\nu}} \tag{1.11}$$

Equation 1.11 shows that when hydrodynamic broadening dominates, resolution scales inversely with the square root of the linear flow velocity and is independent of the electric field strength. The resolution also scales inversely with the channel height, meaning device designs should minimize this factor as much as possible to improve resolving power.

In their work, Fonslow and Bowser also showed that resolution can be efficiently optimized by first finding the separation power that spreads the bands evenly across the separation channel of the device to maximize peak capacity. From here the electric field and linear velocity can be tuned such that the separation power remains constant while minimizing broadening.[2]

The role of surface adsorption on broadening in μFFE separations has been examined by Geiger et al.[8], and it was found to have no impact on resolution. This is because as analytes become fixed to the surfaces of the device, they no longer move due to the pressure driven flow or the electric field. As a result, the only metric altered is the transit time of the analyte through the device. Despite this being of no consequence for a simple μFFE separation, it is a significant issue for some of the technique's applications. Notably, the loss of temporal resolution complicates the ability to continuously monitor changes in an analyte stream over time. Specifically, the loss of temporal resolution reduces the minimum timescale over which changes can be observed. Furthermore, in 2D separations where analytes are introduced into the device as discrete plugs, adsorption further broadens the peak in the time resulting in the potential loss of resolution between peaks from the first dimension.

Electrolysis in µFFE

A significant limitation of µFFE is its high cross-sectional area that leads to higher currents than typical for a microfluidic device, even at low voltages. The high current results in the formation of electrolysis products in the form of bubbles at the electrodes, which can act as insulators that warp the electric field and disrupt stable flow within the device. This disruption leads to the inability to apply electric fields to the device over long periods of time which effectively negates µFFEs ability to continuously separate analytes. Thus, significant considerations must be made to mitigate this limitation such as isolating the electrode channel from the separation channel[3], using deeper electrode channels to quickly eliminate electrolysis products[5], and using buffer additives.[34]

Using channel depth versus flow isolation to mitigate the limitations caused by bubbles divides devices into open and closed channel designs, respectively. Initial closed designs incorporated long and narrow microfabricated channels to act as a pseudo membrane between the electrode channels and the separation channel[7]. However, these channels drastically increase electrical resistance causing a substantial potential loss across the pseudo membrane. As a result, the separation channel experiences less potential drop across it. This leads to low voltage efficiency as the electric field is poorly coupled to the separation process. Other closed designs have incorporated *in situ* polymerization of ion permeable membranes[35–37] within the device which effectively segregates bubbles from the separation channel. However, potential is lost across the membranes resulting in low voltage efficiency. Furthermore, the ion permeable membranes are not chemically stable and periodically need replacement. Several other closed system designs have been utilized such as using a microfabricated wall with a small gap to act as a liquid bridge[38], electrostatic induction[20], and salt bridge

connections.[22] In addition to added fabrication difficulties and reduction in electric field strength, these closed designs also introduce electrodynamic broadening which further reduces their separation efficiency.

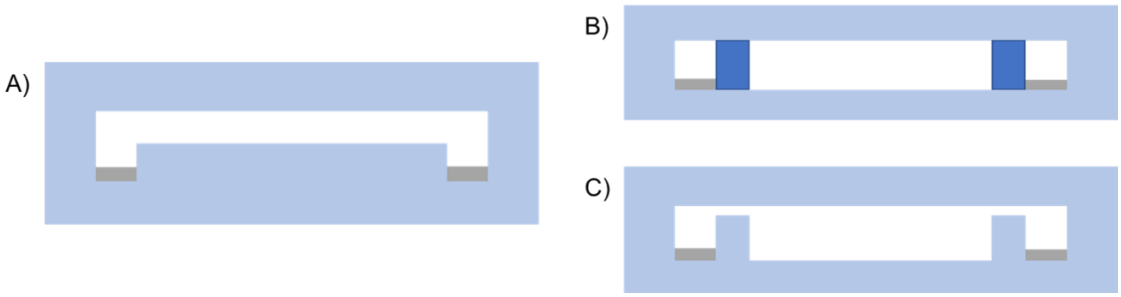

Figure 1.2 A) Side view of an open channel design where the separation channel is not segregated from the electrodes (grey). B) Side view of a closed channel device, where the electrodes are segregated from the electrodes by a structure (blue) typically an ion permeable membrane. C) Side view of a closed channel device where the separation channel is segregated from the electrodes by a wall with a small gap that acts as a liquid bridge to allow ions to flow between the channels.

Open channel devices instead opt for no physical barriers between the electrode and separation channels to avoid potential loss, thus requiring alternative methods to deal with electrolysis products. Open channel devices have used potentials under 2V to prevent the electrolysis of water[14], which while effective drastically limits the separating power of the device. Alternatively, open channel devices have utilized increased electrode channel depth relative to the separation channel to quickly clear electrolysis products before they can disrupt flow.[5] Lubrication theory predicts that a 4× increase in the height of a planar channel will result in 16× higher linear velocity[5]. This increased flow is utilized in a µFFE device by seating the electrodes in a deeper channel, wherein the bubbles due to electrolysis will form in the faster flow streams and be eliminated from the device before they can grow large enough to disrupt stable operation. Lastly, the use of a nano-porous polytetrafluoroethylene (PTFE) membrane as a top cover for a device has been shown to allow the bubbles to be purged from the device while remaining stable at electrical fields of 500 Vcm^{-1} for over three hours of continuous separation.[39]

The addition of buffer additives to mediate electrolysis has been used in open channel designs as an additional means of maintaining stable flow[6,8,23,28,34,40]. The addition of a competing redox pair, hydroquinone and p-benzoquinone, flowed over the electrode channels has been shown to allow field strengths as high as 215 Vcm^{-1} while suppressing bubble formation.[40] This method, however, introduces pH gradients near the electrodes which can negatively affect detection particularly with fluorescence based methods. The addition of surfactants such as Triton x-100 and organic modifiers such as methanol have been shown to improve stream stability as much as 8-fold.[34] The improved stream stability is caused by the additives reducing the surface tension of the water, resulting in smaller electrolysis bubbles that are more easily eliminated from the device. By utilizing both 4× deeper electrode channels and 300 µM Triton x-100 as a buffer additive, Frost and Bowser were able to achieve a stable separation of fluorescein, rhodamine 110, and rhodamine 123 at 40 Vcm^{-1} for 2h.[34] It should be noted, however, that buffer additives can create additional constraints on device design and application as certain device materials are incompatible with methanol and neutral surfactants like Triton x-100 are incompatible with certain detection modes like ESI-MS.

µFFE Detection

Since µFFE's inception detection has been performed predominantly using direct online methods, due in part to the small detection zone and optically clear device substrates. While it is possible to perform offline detection of fractions, as is common for FFE[33,41], the small volumes associated with µFFE have resulted in fractionation seeing little use.[9,25,30] To date µFFE detection has been performed using point source detectors with translational movement[1,7,42], whole device fluorescence imaging [2,7,14,18,19,22,25,34,38]

(Figure 1.2), laser induced fluorescence[23,27,43,44] (LIF), surface enhanced Raman spectroscopy[21] (SERS), and direct coupling with mass spectrometry (MS). [26,29,30]

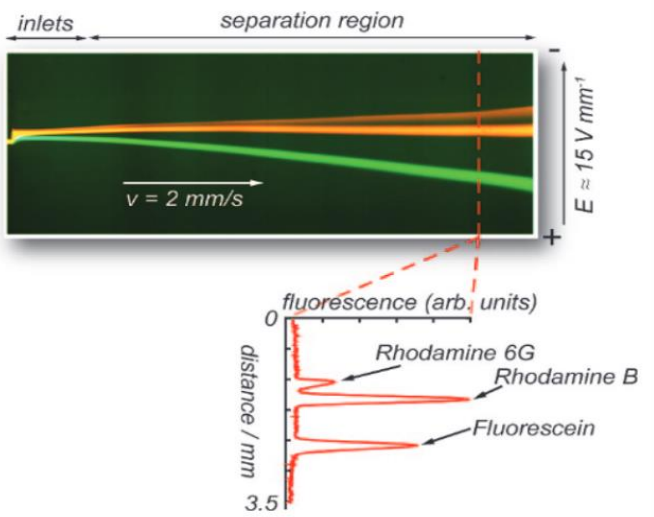

Figure 1.3 Whole chip fluorescence imaging taken on a glass µFFE device showing baseline separation of fluorescein, rhodamine B, and rhodamine 6G. (Image contrast and colors were enhanced by the original authors for better visualization). Adapted with permission from Kohlheyer, D., Eijkel, J. C. T., Schlautmann, S., van den Berg, A., & Schasfoort, R. B. M. (2008). Bubble-free operation of a microfluidic free-flow electrophoresis chip with integrated pt electrodes. *Analytical Chemistry*, *80*(11), 4111–4118. Copyright 2008 American Chemical Society.

Whole device fluorescence detection (Figure 1.3) has seen widespread use as a detection method for µFFE due to its high sensitivity ability to continuously image the entire separation channel.[2,7,14,18,19,22,25,34,38] In this method a lamp is used to excite fluorophores across the entire separation channel. Whole device fluorescence detection allows efficient visualization of sample stream behavior, which can be useful for diagnosing flow problems within a device. When greater sensitivity is required, LIF performed by spreading a laser into a line across the separation channel has been used.[23,27,43,44] Turgeon et al.[43] showed that using LIF detection method, in conjunction with signal averaging, limits of detection for fluorescein as low as 14 pM were achievable.

Becker et al.[21] demonstrated that SERS could be used as a label free detection method for μFFE, using 5-8 μm diameter silver colloids to detect myoglobin using ITP focusing. Though successful, it was observed that agglomeration of the silver colloids occurred near the outlets of the device, obstructing flow. It was hypothesized that laser vacuum deposited silver island films could be used to overcome this issue, but no such device has yet been reported.

Integration of μFFE with MS has long been sought after due to the label free nature of MS and its ability to directly identify the separated analytes.[13] However, coupling the large planar separation channel of μFFE with MS techniques is challenging. Chartogne et al. first demonstrated this was possible using a μFFE device with capillaries fixed in the device as outlets with one capillary acting as the electrospray ionization (ESI) nozzle coupled to the mass spectrometer.[13] This design was limiting as only analytes directed to the coupled outlet could be analyzed by MS. Benz et al.[26] improved upon this design, coupling μFFE to nanospray MS by a single outlet while using multiple buffer inlets that could be manipulated to move analyte streams to the coupled outlet. In this iteration a full scan of the separation channel could be performed in 2.5 minutes. More recently, Jender et al.[29,30] coupled μFFE to ESI-MS using a valve switcher to enable detection of all outlets without flow manipulation. This was accomplished using peristaltic pumps downstream of the μFFE device to ensure even flow at all the outlets with the valve switcher sending effluent from the desired outlet to ESI-MS. However, this design had a two-minute delay when switching outlets leading to long scan times across the device.[30] Jender et al. has since further improved on this design by implementing a multi-emitter electrospray ionization interface that allows a full scan of all outlets in just 6.3s.[29]

µFFE Applications

While µFFE can assess a wide range of analytes with its various separating modes, it has yet to see widespread use largely due to it not performing substantially better than other well established microscale separation techniques. However, the continuous nature of µFFE separations lends itself to unique applications that could lead to more widespread adoption of the technique once they are established and optimized. Namely, the continuous nature of µFFE allows for rapid on-line microscale sample purification[9,13,25,44,45], continuous on-line monitoring of a changing system[46,47], and high efficiency 2D separations when it is used as the second separating mode.[23,27,28]

Two Dimensional Separations with µFFE

Two dimensional (2D) separations are incredibly powerful analytical techniques that involve interfacing two separation techniques, such as gas chromatography (GC) or liquid chromatography (LC), that separate based on different molecular properties to resolve a complex analyte mixture. Common 2D separation techniques include: 2D-gel electrophoresis[48,49], 2D gas chromatography (GC × GC)[50–52], and 2D liquid chromatography (LC × LC).[53–55] Both GC × GC and LC × LC can function as off-line and on-line methods. Off-line methods rely on collecting fractions from the first dimension that are analyzed separately in the second dimension. Commonly, a “heart cutting” technique is used, wherein only specific fractions or peaks from the first dimension are

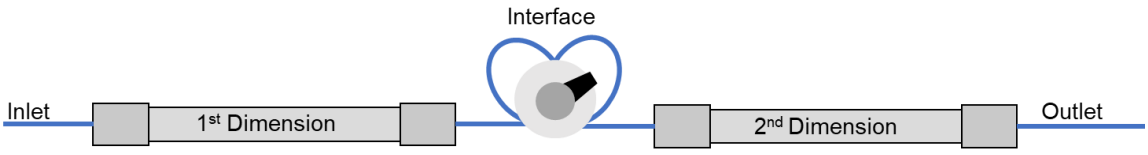

Figure 1.4 Simplified schematic of an on-line LC×LC separation method. Sample and eluent run through the inlet. The effluent from the first dimension of the separation is collected at an interface and injected into the second dimension of the separation. The outlet is connected to the detection method.

analyzed in the second.[50,53] Notably, off-line methods allow the two separating dimensions to be optimized independently. However, fractionation drastically increases analysis time when the entire first dimension needs to be sampled. On-line methods, in contrast, directly interface the two separating modes, allowing the entirety of the first dimension to be sampled by the second with significantly lower analysis times. However, the sampling rate is limited due to the need to complete and re-equilibrate the separation in the second dimension between each sample. Consequently, this often results in very slow separations in the first dimension and sub-optimally short separations in the second dimension to avoid issues that arise due to under sampling.[56]

Under sampling occurs due to the need to collect discrete plugs from the first dimension of the separation that can then be sent to the second separating dimension. Murphy, Schure, and Foley demonstrated that a first-dimension peak must be sampled three to four times over its 8σ baseline width to avoid serious loss of resolution and peak capacity of the separation when the first dimension contributes heavily to resolution[57]. This means that for a 2D LC separation where the cycle time of the second dimension is 12 seconds[56], the peaks must have an 8σ baseline width of at least 48 seconds in the first dimension to avoid loss of peak capacity and resolution. The continuous nature of µFFE separations, however, effectively eliminates under sampling as an issue since a peak from the first dimension will be sampled a number of times equal to the peaks width divided by the sampling rate of the µFFE detection method. For example, a liquid chromatography coupled to µFFE (LC × µFFE) separation using a CCD with a 200 ms exposure time for µFFE detection would be able to effectively sample a peak from the first dimension with an 8σ baseline width of 0.8 seconds, which is narrower than would be expected even for most unretained peaks.

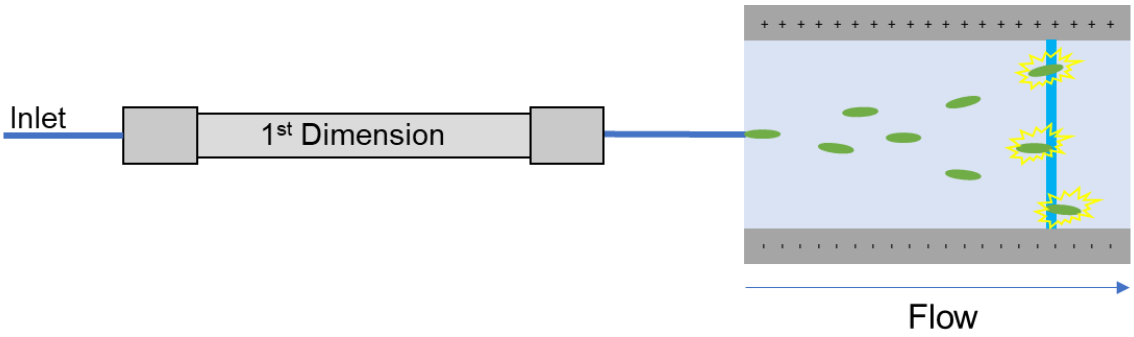

Figure 1.5 Simplified schematic of an LC × µFFE separation method. Sample and eluent are introduced the LC column via the inlet. All effluent coming from the LC streams directly into the µFFE device with no intermediate sample collection.

Geiger et. al. demonstrated to power of µFFE in two dimensional separations by coupling nano-liquid chromatography (nLC) with µFFE (nLC × µFFE) for the separation of peptides[27] and amino acids.[28] The two separating modes were interfaced using a capillary that fed sample directly into the µFFE device to minimize dead volume that would result in loss of resolution due to remixing. In the separation of fluorescently labeled BSA tryptic digest an ideal peak capacity of 2352 was achieved in a 10 min separation window (235 peaks/min).[27] With the variety of nLC stationary phases that are commercially available in combination with the different µFFE separating modes, Geiger et al. suggested that nLC × µFFE could be applied to a wide variety of analyte mixtures.

Johnson and Bowser similarly demonstrated the capability of µFFE in two dimensional separations by coupling CE with µFFE for the separation of fluorescently labeled amino acids and peptides.[23] The CE separation was performed on a capillary that was directly interfaced with the µFFE device to minimize the dead volume. The EOF used to drive flow in the CE dimension of the separation only generated a flow rate of 86 nL/min, substantially slower than the 300 nL/min used by Geiger et al. Johnson and Bowser demonstrated that this resulted in no significant broadening at the interface between the capillary and µFFE device, as it was easily able to clear the approximately 1 nL dead volume before remixing could occur. Since CE and µFFE both separate

analytes based on electrophoretic mobility different buffer pHs were used to vary analyte charges between the two separation modes (pH = 10.01 in CE and pH = 5.2 in µFFE). Additionally, 35 mM α-cyclodextrin was used as an additive in the CE buffer to further differentiate the two modes. In the separation of a fluorescently labeled BSA tryptic digest an ideal peak capacity of 2592 was achieved in a 7.2 min separation window (342 peaks/min).[23] Like nLC, numerous other separating modes for CE such as micellar electrokinetic chromatography (MEKC), affinity capillary electrophoresis (ACE), and IEF in combination with the different µFFE separating modes could be used to expand the analyte mixtures CE × µFFE could be used to analyze and further differentiate the separation between the two dimensions.

Further applications of 2D separations utilizing the continuous nature of µFFE separations have yet to be developed. However, with the ever-increasing complexity of analyte mixtures, particularly within omics fields, the potential value of such powerful multi-dimensional separation tools will only grow. Particularly, with the advances of Jender et al.[29] efficiently coupling µFFE with MS, the possibility of a comprehensive nLC/CE × µFFE × ESI-MS separation for the analysis of complex biological mixtures presents a challenging but appealing opportunity.

Microscale Sample Purification

The small volumes, low sample flow rates (86-3000 nL/min [9,23,28,44,46,58]), and continuous nature of µFFE separation allow it to be used for sample purification at a microliter scale on a relatively fast timescale. In particular, µFFE has been used for buffer exchange[13], solvent exchange[45], the monitoring and purification of on-line reactions[25], and the isolation of DNA aptamers.[9] For µFFE, samples are often collected as fractions at the separation channel outlets and processed offline[9,25]. However, in

cases where a downstream detection is performed the sample is directed to the desired outlet by electrophoretic deflection[13,45] or buffer flow rate manipulation.[26]

Chartogne et al. coupled capillary isoelectric focusing (cIEF) with µFFE and ESI-MS on-line for the analysis of myoglobin, carbonic anhydrase I, and β-lactoglobulin.[13] µFFE was used to remove the carrier ampholytes necessary for focusing in cIEF. The removal of ampholytes was critical since their presence in high concentrations results in reduced sensitivity in ESI-MS due to ion suppression[59,60] and can result in salt build-up on at the electrospray interface.[61] Since analytes entering the µFFE device had no charge, a 1% acetic acid solution was used as the separation buffer to quickly cause the proteins to gain a positive charge and be deflected towards the desired outlet. Chartogne et al. noted that sample dilution and peak broadening during the µFFE step could lead to poor performance in ESI-MS. To resolve this, future work should implement a higher number of outlets to reduce dilution and improve ampholyte elimination from the sample.

Zitzmann et al. utilized µFFE to perform a solvent exchange, moving fluorescein from an organic solvent, dimethyl sulfoxide (DMSO), to an aqueous solution.[45] Using a three-inlet design, one inlet for sample introduction and two for running buffer, with carefully optimized ratios between the flow rates 95% of the DMSO was effectively removed from the fluorescein sample. Combined with the dilution factor of 5, this resulted in a sample solution containing only 1% DMSO. Zitzmann et al. noted that other organic solvents with good miscibility with the aqueous phase, such as methanol or acetone, could be used, and that this method has potential applications for on-line multistep synthesis where solvent exchange is necessary.

Jing et al. demonstrated that μFFE can be used to isolate DNA aptamers for human IgE using Selective Evolution of Ligands by EXponential enrichment (SELEX).[9] The use of μFFE to perform SELEX brings significant advantages over other aptamer selections like CE-SELEX due to the ability to continuously introduce, separate, and collect the bound aptamers. CE-SELEX only allows for several nL of sample to be injected at a time[62], limiting the number of sequences that can be assessed and requiring high DNA library concentrations. Jing et al were able to use μFFE to assess 1.8×10^{14} sequences in a single round, a 300-fold improvement over CE-SELEX. Furthermore, the authors were able to select an aptamer with high affinity (K_d = 20 nM) within just 2-4 rounds of enrichment.

Kostal et al. were able to rapidly determine the electrophoretic mobility of mitochondria from rat myoblasts using μFFE.[44] The authors were able to use approximately 100-fold less sample, 10-fold less buffer, and were able to use a 15-fold lower electric field compared to FFE. In addition, a sample could be analyzed in less than 30 seconds which was substantially shorter than both macroscale FFE and CE methods which take approximately 25 minutes. Kostal et al. noted that though μFFE has significant benefits, CE with LIF detection offers lower limits of detection which is essential for the analysis of individual mitochondrion properties.

Pfeiffer et al. demonstrated μFFE's ability to continuously purify the products of an organic synthesis.[25] The target reaction in this purification produced triarylmethanes which are lead structures used in the synthesis of dyes and drug candidates[63]. Specifically, 1-napthol, benzhydryl alcohol, and triarylmethane were separated. Deep-UV fluorescence was used to continuously monitor stream positions while fractions were

collected from each outlet. Each fraction was then subsequently analyzed via CE which confirmed the presence of only one component and buffer in every fraction.

Continuous Online Monitoring

The continuous nature of µFFE separation makes it uniquely suited for use in applications where online monitoring of a separation is desired. Whereas other methods of monitoring require discrete injections of sample that are limited by the speed of the separation, µFFE detection is only limited by the exposure time of the detection method. As a result, µFFE can respond to analyte changes at a rate of 100 ms or less[43], enabling quick separation optimization[47] and measurement of equilibrium constants.[46]

Fonslow and Bowser utilized µFFE with a buffer additive gradient to accomplish both quick separation optimization and equilibrium constant estimation[47]. The experiment utilized a mixing tee to create a separation buffer with a hydroxypropyl-β-cyclodextrin (HP-β-CD) concentration that varied from 0-50 mM over 5 min. The HP-β-CD containing buffer was used to separate NBD-F labeled glycine, L-serine, and phosphorylethanolamine (PEA). Scans of the separation were recorded every 5 seconds, assessing the resolution of the separation at 60 different HP-β-CD concentrations to find the optimal conditions. This data was also used to estimate the dissociation constant (K_D) between the HP-β-CD and primary amine analytes which were subsequently compared to values determined by CE. While the K_D values for L-serine were indistinguishable between the two methods, the values for glycine and PEA were noticeably lower in the µFFE separation. This discrepancy was hypothesized to be a result of the K_D plots not plateauing due to the gradient not testing a wide enough range of HP-β-CD concentrations.

Turgeon et al. similarly used a gradient in µFFE to measure aptamer-ligand equilibria.[46] This experiment utilized a mixing cross to generate a gradient in human IgE concentration in a sample that contained a fluorescently labeled aptamer specific to human IgE and an internal standard. This sample mixture was then allowed to equilibrate over 4 min within a PEEK capillary as it was pumped to the µFFE device. The gradient was generated over 5 min covering a range of 0-500 nM IgE, with images taken of the separation every 1 s resulting in data at 300 different IgE concentrations. An internal standard was used to determine the IgE concentration at each point when generating the binding curve, as this made the generation of a perfectly linear gradient unnecessary. Through this method Turgeon et al. were able to determine a dissociation constant of 48 $\pm$ 3 nM, similar to the value determined by a subsequent fluorescence polarization assay and a previously published value determined using affinity capillary electrophoresis (ACE).[64] Notably, gradient µFFE provided much higher throughput than other methods, generating a substantial amount of data in only 5 minutes that would have taken hours to obtain via CE methods.

µFFE Design and Fabrication

The materials used to fabricate µFFE devices are chosen based on several factors: optical properties, electrical properties, surface chemistry, and ease of fabrication. High optical transparency is generally a necessity to enable efficient detection of analytes within the device. The material must be a good insulator to prevent current from flowing through the device. The surface of the material should be neutral to prevent electroosmotic flow during operation while ideally being hydrophilic to facilitate efficient removal of electrolysis products from the device. While the surface chemistry of a material is important, in many cases the surface chemistry of a material can be

modified, sometimes permanently. With few exceptions, the device material chosen should be the first and most important factor when designing a µFFE device as the material properties can significantly impact the design, fabrication, performance characteristics, and possible applications of the device.

µFFE Device Materials

µFFE devices have been fabricated in a wide range of materials, with the first devices being fabricated in silicon by Raymond et al.[1] Despite successful use of these devices to perform proof of concept separations, silicon was shown to be a poor material for µFFE fabrication. Notably, silicon is a conductive substrate. Consequently, the device required an insulating layer to be deposited on it to prevent current from flowing through the material during operation.

Poly-dimethyl siloxane (PDMS) is a material commonly used for microfluidic devices due to its low cost and ease of fabrication.[12,19,22,65,66] For µFFE devices, PDMS also allows for cheap and quick fabrication with channel heights as low as 10 µm.[12,67] PDMS, however, has a few undesirable qualities that has limited its use as a material for µFFE devices. The low aspect ratio of the separation channel in µFFE devices, in combination with the elasticity of PDMS, causes the channel to bow out or collapse when positive or negative pressure is applied, respectively. PDMS µFFE devices have incorporated separation channel posts to prevent channel distortion, however these occupy a significant volume and reduce the effective width available for separation. In addition to elasticity, the hydrophobicity of PDMS poses a problem for µFFE devices as it complicates bubble-free filling by aqueous solutions and subsequent removal of bubbles generated via electrolysis. Furthermore, the hydrophobic surface can lead to non-specific adsorption of proteins and other molecules like therapeutic drugs.[68] These

issues can be mitigated by a variety of different treatments to make the PDMS surface hydrophilic; however, PDMS can quickly recover its hydrophobicity resulting in the need for frequent treatment of the device.[69,70]

Glass has been a widely used material for µFFE devices[2–5,8,16,23,47,71] as it possesses high optical transparency enabling efficient detection. It is also a good insulator allowing substantially higher voltages to be applied when compared to silicon[4]. The material is also rigid preventing the deformation of channel structure when pressure is applied to drive flow. Furthermore, the surface of glass is hydrophilic, making removal of bubbles generated in the device during operation easier. While glass is a useful µFFE device material, it's surface commonly carries a charge and thus requires treatment to suppress EOF, prevent surface adsorption, and ensure consistent surface chemistry within the device.[2,23,27] Fabrication in glass is also time consuming and expensive compared to fabrication in other materials, requiring specialized instrumentation and facilities for much of the process.

Several rigid polymers have been used to fabricate µFFE devices including poly methyl methacrylate (PMMA)[18], acrylonitrile butadiene styrene (ABS)[6], polytetrafluoroethylene (PTFE) combined with polycarbonate (PC)[13], cyclic olefin polymer (COP)[38], and cyclic olefin copolymer (COC).[72] Rigid polymers provide a compromise between glass and PDMS, being faster and cheaper to produce than glass devices without the need for frequent surface treatment. In addition, rigid polymers enable the use of a variety of fabrication methods like 3D-printing[6], injection molding[38], and hot embossing.

Polymers such as PMMA and ABS have significant issues as µFFE device materials and are largely used due to their advantageous fabrication methods.[6,18] Both

PMMA and ABS can adsorb water which can lead to humidity negatively impacting reproducibility in devices and performance. Specifically, ABS undergoes cycles of wetting and drying that cause cracking of the material surface.[6] These cracks greatly interfere with both flow paths in the device and with efficient detection. Consequently, ABS devices have short lifetimes. Even when stored with water in their channels to minimize drying and wetting cycles ABS devices only have a lifetime of several weeks.[6]

Over the past decades, COC and COP have become widely used in the production of microfluidic devices due to their desirable surface chemistry and optical properties. COC and COP are highly similar in their properties, with COC generally being favored due to its lower cost. In addition to being cheap and rigid, COC has high optical clarity and low background fluorescence which allows for efficient sample detection.[73] COC is also resistant to acids, bases, and most polar organic solvents. In addition, COC has extremely low water absorption (<0.01%) which results in humidity having little to no effect on reproducibility.[74] With regards to µFFE, the major complication of COC as a device material is its hydrophobicity which complicates bubble free filling and removal of electrolysis products. However, the surface of COC can be modified to be hydrophilic by photografting[75] and plasma treatment[76] without the need for frequent retreatment.

Fabrication Methods

Fabrication of µFFE devices typically involves the creation of two or more patterned parts that are sealed together to form the channel structure and fluidic access ports of the device. Sealing the device can be as simple as carefully placing the device on a glass slide for PDMS devices[65], or it can require complex instrumentation to deposit thin films and anodically bond the parts together like with glass.[4] Both the sealing and

fabrication method are highly dependent on the device material and should be considered when determining which device material to use.

Wet etching, in combination with photolithography, is the predominant method for fabricating μFFE channels in glass.[4,5,8,9,23,27,28,43,46,77] In this process the wafer is cleaned with piranha solution and a thin masking layer of chromium and gold are deposited on both sides of the substrate. A layer of photoresist is spun over the metal masks, and selectively cured on one side with a mask to produce the desired pattern. The exposed photoresist is then removed and the chromium and gold layer beneath etched off with metal specific etchants. The wafer is then submerged into concentrated HF to etch the channels into the exposed substrate. This process can then be repeated using a different mask to produce multiple different channel heights.[5] Device production using wet etching can be a relatively long and expensive process, making it a poor fabrication method where rapid iteration of designs is desired.

Once the channels have been etched, the device needs to be sealed to another glass wafer with fluidic access holes. This has been accomplished in three ways for glass μFFE devices: thermal bonding[10,78], anodic bonding[4], and photolithography.[36,37] Thermal bonding is a process in which the two substrates are placed under pressure at temperatures near or above their glass transition temperature over long time periods to anneal them together. This method produces strong bonds; however, it can generate interfacial stress between the wafers and cause sagging in the low aspect ratio separation channel. Sagging limits the height of the channel to 30 μm with smaller channel heights likely requiring supports to prevent collapse and deformation[78].

Anodic bonding is a technique that utilizes high temperatures and an applied voltage to generate a sodium-depleted region at the material surface to promote

electrostatic interactions between two substrates. The electrostatic interactions then facilitate anodic oxidation, creating chemical bonds between the substrates. For a glass-to-glass bond a thin layer of amorphous silicon can be used as an intermediary layer to act as the oxidizable material and sodium ion barrier to facilitate the process.[79] Anodic bonding notably uses temperatures well below the glass transition temperature of the material, eliminating the risk of sagging and enabling the fabrication of glass µFFE devices with channel heights below 30 µm.[4]

Glass µFFE devices have also been fully fabricated and sealed using photolithography with photo curable polymers[36] or monomers.[37] These methods utilize a thin layer of photocurable material sandwiched between two glass substrates, one containing holes to enable fluidic connections. A mask is then used to selectively expose the polymer, curing the exposed material to generate all or part of the channel structures and annealing the substrates together. Excess uncured polymer is then washed out of the device. This method can produce channel heights as low as 25 µm[36,37], but cannot generate different channel heights without etching the glass substrates.[37]

Soft lithography is a fabrication technique that is widely used for the fabrication of PDMS microfluidic devices. This technique involves coating a wafer in photoresist, selectively curing a portion of the resist with UV light and washing away uncured photoresist with a developing solution. The resulting wafer is a negative of the channel design, functioning as a master mold for device production. PDMS base and catalyst are then mixed and poured over the master mold. The polymer is degassed and cured before being removed from the mold to produce the channel half of the device. Holes are then punched in the PDMS to enable fluidic access, and the device half is then

sealed by simply placing it on a glass substrate.[12,65] If pressures great enough to break this seal are required during device operation, the PDMS can be cross-linked to the glass by plasma exposure.[66]

Spacer based fabrication is a method for producing µFFE devices in rigid polymers. This method utilizes a patterned spacer material to separate a top and bottom substrate to generate the channel structure. Chartogne et al. were the first to fabricate a µFFE device in this way by sandwiching a polytetrafluoroethylene film with the channel structure cutout between two machined polycarbonate plates.[13] The device was then sealed by screwing them together tightly, with the center screws on either side serving as the electrode. Notably, channel height was determined by the thickness of the sandwiched film, resulting in a separation channel height of 100 µm. This method was expanded upon by Walowski et al. using two layers of laser cut transfer-adhesive tape as the spacer to generate the channel structure.[18] The use of two spacers enabled the fabrication of a more complex design that included partition bars between the electrode and separation channels. The use of transfer-adhesive tape also reduced the separation channel height to just 50 µm.

Injection molding is a method of fabrication that injects a polymer melt into a mold and then cooled to solidify the polymer in the desired shape. The wide range of available fabrication materials, high replication accuracy, and high throughput of injection molding make it highly desirable for parts that need large production volumes while maintaining high levels of precision.[80] As a result, injection molding sees significant use in microfluidic device fabrication, particularly in materials like COP and COC.[81–83] However, the need for expensive molds leaves injection molding poorly suited for settings where rapid changes of device design are desired. Köhler et al. took advantage

of injection molding to produce a COP µFFE device based off a previous PDMS design.[38] Integrated and external electrode designs were explored, with integrated electrodes notably being laborious to implement and eliminating the potential for mass fabrication. External electrodes were found to have significantly lower voltage efficiency than integrated electrodes. However, it was noted that there was no significant difference in the separations between the different designs besides the applied voltage. While µFFE does not currently demand high production volumes, widespread adoption of the technique could cause injection molding to become a dominant fabrication method used for commercial production of devices.

Hot embossing is another technique frequently used to fabricate microfluidic devices in rigid polymers like COP and COC.[84–86] In hot embossing, a mold that is a negative of the desired features is placed into contact with a substrate, heated above the substrate glass transition temperature, and put under pressure to imprint the mold into the substrate. The mold and substrate are then cooled below the glass transition temperature of the substrate, the pressure is removed, and the mold and substrate are separated. Like injection molding, hot embossing has a wide range of viable materials, high replication accuracy, and is capable of high throughput. Additionally, hot embossing has less warping and shrinkage of the fabricated piece than injection molding.[80] Mold fabrication techniques are often laborious and expensive, requiring clean rooms or micromachining, making hot embossing poorly suited for work where rapid changes in design are necessary. The first fabrication of a µFFE device via hot embossing is presented in Chapter 4.

With the development and advancement of 3D printing technology came new methods of fast and inexpensive fabrication of parts. With 3D printing becoming more

widely accessible and its ability to rapidly change and produce designs for little cost it has seen significant use in the production of microfluidic devices.[6,87–95] There are several different modes of 3D printing, such as fused deposition modeling (FDM), stereolithography (SLA), and poly-jet 3D printing. The modes each have a variety of materials they can fabricate in and have different limitations associated with them.

FDM utilizes melted or thermally softened plastics or metals to deposit lines of substrate that fuse together to form 3D objects. Substrate is fed to a nozzle that heats and melts the material which is forced out onto a printing bed to form the base layer of the object. The printing bed or nozzle is then lowered or raised to enable fabrication of subsequent layers.[96] FDM 3D printing can produce layers as small as 20 µm with a XY resolution of as little 25 µm depending on the printer. Furthermore, it has a wide range of materials available with some of the most common being polylactic acid (PLA) and ABS. Notably, FDM 3D printing was utilized by Anciaux et al. to produce an ABS µFFE device.[6] The µFFE device had a separation channel height of 80 µm, however, artifacts

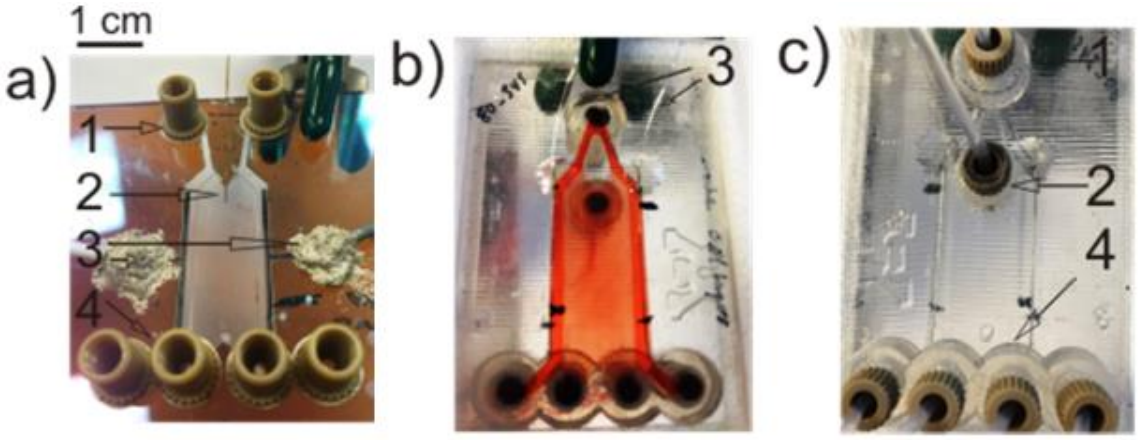

Figure 1.6 Images of a (a) glass device, (b) 3D-printed µFFE device taken from the channel/detection side, and (c) 3D-printed µFFE device taken from the fluidic connection side. Labels highlight (1) buffer inlets, (2) sample inlet, (3) electrode connections, and (4) buffer outlets. Channels were filled with food dye in panel b to demonstrate that no leaking was observed after solvent vapor bonding. Adapted with permission from Anciaux, S. K., Geiger, M., & Bowser, M. T. (2016). 3D Printed Micro Free-Flow Electrophoresis Device. *Analytical Chemistry*, *88*(15), 7675–7682. Copyright 2016 American Chemistry Society.

from 3D printing in the form of print lines, which can be seen in panel c of Figure 1.6, resulted in significant surface roughness. While this was mitigated by acetone vapor exposure in post-processing, the surface roughness was still sufficient to negatively affect detection on the device.

SLA 3D printing utilizes photocurable polymer that is selectively exposed to produce a patterned layer of polymer. The build stage is moved, and subsequent layers of polymer are cured to produce 3D objects.[97] Due to its reliance on photocurable polymers, the pool of materials is limited relative to FDM 3D printing. However, SLA can produce sealed devices in a single step making it particularly desirable for microfluidic device fabrication, so much so that specialized SLA 3D printers are produced for this purpose. Typical SLA 3D printers are capable of layer heights as low as 25 µm with an XY resolution of 25 µm, with high end printers capable of single micron layer height and sub-micron resolution. SLA 3D printing also has lower surface roughness than FDM and print lines are less noticeable, though still present. Despite its advantages over FDM, SLA has yet to be used to fabricate µFFE devices due to the low aspect ratio of the separation channel and the need to integrate electrodes preventing easy one step fabrication.

Poly-jet 3D printing utilizes a print head that sprays droplets of photocurable polymer onto the printing bed. A lamp attached to the print head is used to cure the lines of polymer as it prints.[98] Poly-jet methods can have layer heights as low as 16 µm depending on the material used and XY resolutions around 40 µm. The major advantages of poly-jet 3D printing are the ability to print in multiple materials simultaneously, high throughput, and smooth finishes. However, poly-jet 3D printing has low replication accuracy for structures below 200 µm in the XY plane[87] and is generally

more expensive than typical SLA or FDM printing methods. As a result, no µFFE devices and very few microfluidic devices have been produced using this fabrication method to date; however, further advances in poly jet printing technology increasing accuracy for low micrometer structures could change this.

The sealing of rigid polymer devices is commonly done using thermal fusion bonding[99], solvent bonding[100], and thermal assisted solvent bonding.[101] Thermal fusion bonding is largely the same as it is for glass, wherein the two substrates are placed in contact under pressure and heated near or above their glass transition temperature to form the bond. When thermally bonding, conditions need to be carefully optimized to avoid channel deformation. In channels that have low aspect ratios, like the separation channel in µFFE devices, there is a significant risk of deformation via sagging of the material.

Solvent bonding relies on using solvent, either through vapor or direct exposure, to activate the polymer chains on the surface. These activated chains are semi-mobile and become entangled when pressed into contact with another activated surface. As the solvent evaporates off the chains become rigid binding the surfaces together.[100] Without careful solvent or solvent mixture selection, solvent bonding can cause channel distortion and can trap pockets of solvent in the bond that weaken it over time.

Solvent assisted thermal bonding is a sealing method that uses solvent to activate the surface of the polymer part. The parts are placed in contact under pressure at an elevated temperature, which quickly drives the solvent off to bond the parts together.[101,102] Relative to thermal bonding, this method uses lower temperatures which reduces the risk of channel deformation while taking less time making it more desirable for scalable fabrication processes. Similarly, relative to solvent bonding, less solvent

exposure is required to produce a strong bond which reduces the likelihood of channel distortion.

µFFE Design

µFFE devices have several fundamental features to them, notably, a large planar separation channel, electrodes, separation buffer inlets, sample inlets, and outlets. When designing a µFFE device the most important factors to consider are the height of the separation channel, which heavily impacts sample broadening, and how electrolysis products will be mediated to maintain stable flow in the device. Separation channel height is largely determined by the fabrication material and method and should generally be kept as low as possible. What means of electrolysis product mediation are used in a design should be weighed based on their compatibility with a device material and the desired application of the device.

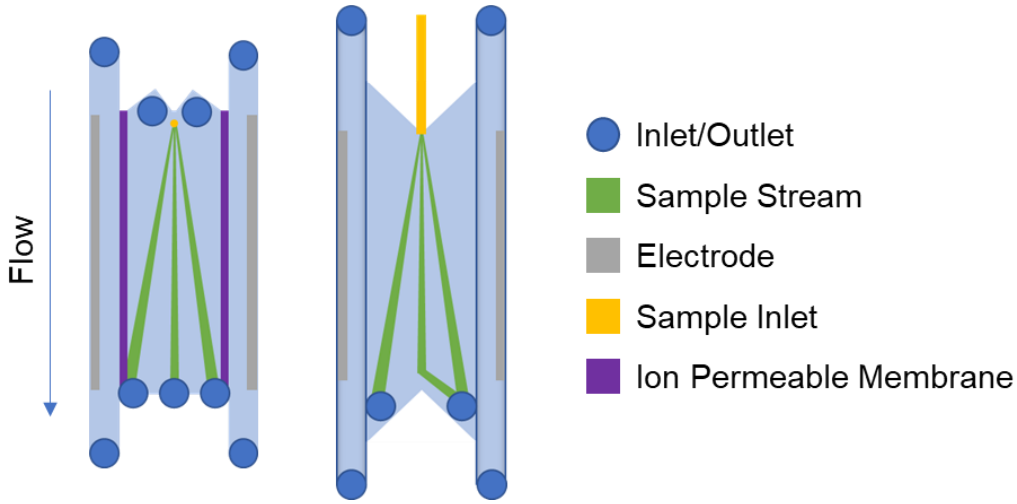

Figure 1.7 General schematic of a closed (left) and open (right) channel µFFE design featuring differing numbers of inlets and outlets. The closed channel design introduces sample to the separation channel through a hole in the top of the device. The open channel design introduces sample to the separation channel via a capillary fed through the side of the device that exits directly into the channel.

Beyond channel height and electrolysis product mediation, the number of buffer inlets, outlets, and how the sample stream is introduced into the device should also be

carefully considered. The number of buffer inlets are generally minimized in a device with many designs only featuring one or two (Figure 1.6). However, there are scenarios where additional inlets are necessary. For example, when using µFFE to perform IEF, it can be necessary to utilize additional inlets to pre-sort the ampholytes by introducing them at different points in the separation channel.[11] The number of outlets heavily depends on the desired application, but commonly designs will have four to six outlets. Increasing the number of outlets can be advantageous when performing analysis downstream from the µFFE device, since this decreases the dilution factor of the sample. Jender et al. notably used 15 outlets when interfacing µFFE with an electrospray ionization multi-emitter.[29] Lastly, the way the sample stream is introduced is important as the injection width plays a role in the band width of analytes, though it is rarely the determining factor. More importantly, how the sample is brought into the device can introduce dead volume that interferes with multi-dimensional separations and continuous monitoring applications. Specifically, when using µFFE downstream of other separations the introduction of dead volume between them can cause remixing that results in significant temporal broadening and reduced resolution.

Scope of Thesis

With the further development of omics fields creating an increasing desire to analyze complex biological mixtures, the advancement of µFFE as a separation technique is of particular importance due to the unique applications it offers. µFFE's potential for high capacity two or even three-dimensional separations, microscale sample purification, and continuous monitoring represents a substantial boon to these fields. In Chapter 2 I will evaluate the potential of utilizing laser light brought in directly from the side of the µFFE, and the potential improvement in detection efficiency and

device design considerations that come with it. Chapter 3 will discuss my attempts to model and develop µFFE designs for the purposes of on-line buffer exchange. Specifically, with the intentions of interfacing strong cation exchange chromatography with ESI-MS for the purposes of enabling a multi-attribute method of analysis for therapeutic monoclonal antibodies. In Chapter 4 I will detail the development of a new fabrication method for µFFE using hot embossing with a poly-jet 3D printed master mold. The use of hot embossing in particular enables fabrication in high performance polymers like COC and the potential for high throughput production. Meanwhile, the use of the 3D printed master molds aims to decrease costs and takes advantage of its ability to rapidly alter and iterate designs.

Chapter 2

Evaluation of Laser Alignment on Laser Induced Fluorescence Detection in Glass and Acrylonitrile Butadiene Styrene Micro Free Flow Electrophoresis Devices

Summary

While most analytical separations are time based, micro free flow electrophoresis (μFFE) separates analytes in space across a separation channel allowing continual injection, separation, and detection of analytes. Consequently, μFFE is capable of continuous analysis, making it an appealing technique for the analysis of biological systems over time. With many biological analytes existing in low concentrations, the improvement of μFFE detection is paramount for realizing its full potential. The most common and most sensitive detection method for μFFE is laser induced fluorescence (LIF) with the laser being spread into a line and reflected onto the device at an angle.

In this chapter the potential of a laser alignment that brings the laser directly through the side of the μFFE device is explored as a means of improving sensitivity. Standard curves were constructed for fluorescein in a glass μFFE device for both top-down and side-on laser alignments. A standard curve for fluorescein in an acrylonitrile butadiene styrene (ABS) μFFE device was also created for top-down laser alignment. Results were unable to be obtained for the ABS device in a side-on laser alignment due to excessive scattering of the laser light. Detection limits for fluorescein were found to be 1.3 and 2 nM for top-down alignment in the glass and ABS device, respectively. The detection limit for fluorescein was found to be 0.5 nM for side-on alignment in the glass device, resulting in an approximately 62% improvement when compared to top-down alignment. This reported improvement is promising, showing that with further work optimizing LIF detection schemes for μFFE is a worthwhile endeavor.

Introduction

The concentrations of biological analytes can range wildly depending on what is being studied, ranging from mM concentrations[103] all the way down to single molecule detection.[104] Consequently, improving the limits of detection (LOD) for an analytical technique can drastically expand the biology it can analyze and increase its potential applications. To this end, improvements in LOD should be sought whenever necessary or possible, especially in relatively new techniques like µFFE which have significant room for improvement and optimization. There are several detection methods for µFFE including whole chip fluorescence [3,12,16,36,40] and MS[13,26,29,30], however the most sensitive method currently available is laser induced fluorescence (LIF).[4,6,23,27,43,47] A typical LOD for fluorescein when using µFFE with LIF detection ranges from around 0.6-5 nM depending on the device material and design.[6] However, when highly optimized using techniques like signal averaging, a LOD as low as 14 pM for fluorescein can be achieved.[43]

Current LIF alignments involves spreading the laser light into a line and reflecting it down onto the device at an angle.[6,23] While effective, spreading the laser light into a line also spreads the laser power density across that line, resulting in less efficient fluorophore excitation. This top-down laser alignment also has the potential to scatter light due to defects on the surface of the device, resulting in increased noise. In this chapter an alternative laser alignment which focuses the laser light through the side of the device is assessed for both a glass and 3D printed ABS device as a means of improving LOD in µFFE.

Experimental

Buffers and Solutions

All solutions were prepared in deionized water (Milli-Q details) and filtered through a 0.22 µm nitrocellulose membrane filter (Fischer Scientific, Fairlawn, NJ). The separation buffer used to generate bulk flow within the µFFE device consisted of 25 mM 4-(2-hydroxyethyl)-1-piperazineethanesulfonic acid (HEPES, Sigma-Aldrich, St. Louis, MO) and 300 µM Triton X-100 (Sigma-Aldrich, St. Louis) with the pH adjusted to 7.00. Fluorescein (Sigma-Aldrich, St. Louis) samples were produced by dissolving in HPLC grade methanol (Thermo Fisher, Waltham, MA) and serial diluting with separation buffer.

Device Fabrication

ABS devices were fabricated based on work done by Anciaux et al.[6] The device was designed in two halves in Autodesk Inventor. The top half featured threaded fluidic connection ports for the buffer inlets and outlets. The bottom featured an 80 µm deep, 1 cm wide, and 2.5 cm long separation channel, two 345 µm deep electrode channels, and

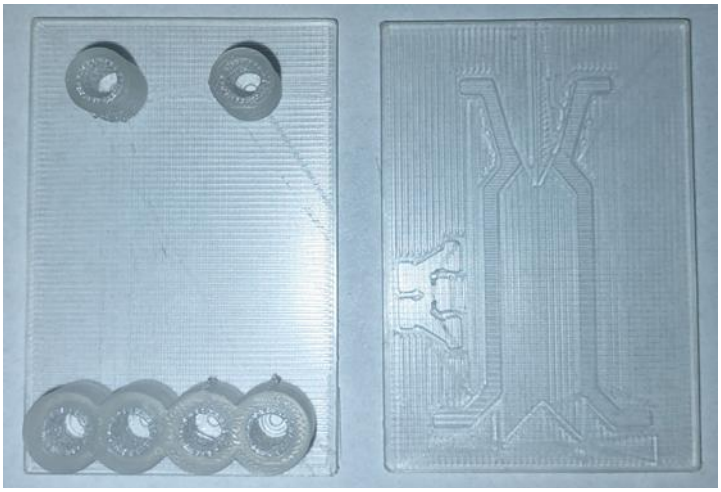

Figure 2.1 Top (left) and bottom (right) of a µFFE device 3D printed in ABS. Holes are drilled into the bottom half and electrodes fixed into the side channels. The halves are exposed to acetone vapor, the capillary is aligned between them, and the halves are pressed together to seal the device.

a 2 cm long, 300 µm wide, and 150 µm deep sample channel. Both halves were printed simultaneously using an Ultimaker^2 FDM 3D printer with a 0.4 mm diameter nozzle. The print was performed using the following conditions: 260 °C nozzle temperature, 90 °C printing bed temperature, 10 mm/s printing speed, 20 µm layer height, and 106% material flow rate. Devices were printed in 2.85 mm diameter Transparent Premium ABS filament (Matterhackers, Lake Forest, CA). Electrode holes were drilled at a 30° angle into the tops of the electrode channels using a 400 µm bit and drill press (Micro-Mark, Berkeley Heights, NJ). Two approximately 5 cm long 250 µm diameter platinum wires (99.99%, Sigma-Aldrich, St Louis) were inserted through the electrode holes and were fixed to the bottom of the electrode channels by carefully melting them into the ABS using a soldering iron.

Device halves were sealed by solvent assisted bonding using acetone vapor to activate the polymer surface. Acetone vapor exposure was performed in a fume hood by heating acetone in a Pyrex beaker on a hot plate to 90 °C. Acetone is flammable and caution needs to be taken while heating it. The half containing the channels was suspended in the acetone vapor feature side down, exposed for 1.5-2 min, and allowed to dry for 2-3 min prior to bonding. While the channel half dried, the fluidic access half of the device was suspended in the acetone vapor port side up, exposed for approximately 1 min, and allowed to dry for approximately 1 min before bonding. After drying, the 30 cm long, 300µm o.d., 20µm i.d. capillary was seated in the sample channel and the two halves were aligned. Bonding was performed by hand by lightly pressing the device halves together along their sides. The electrode holes were sealed using quickset epoxy. The device was left to dry overnight at room temperature prior to use. Small copper alligator clips and lead wires were used to make electrical connections with the

electrodes. After initial filling, devices were stored with water in the channels to prevent the surface of the channels from drying out and cracking.

Glass Devices were fabricated based on a procedure described by Fonslow et al.[5] A 1.1 mm boroflat wafer was first cleaned with Piranha solution before photolithography techniques were used in conjunction with wet etching to produce 60 µm deep electrode channels. After unmasking, a second round of photolithography and wet etching was performed resulting in a 20 µm deep separation channel and 80 µm deep electrode channels. A Temscal electron beam evaporation system was then used to deposit 100 nm of Titanium followed by 150 nm of gold. Photolithography was then used to pattern the electrodes and the unprotected metal was removed using metal etchants. A second wafer then had 1 mm access holes drilled using a diamond tipped bit to create the buffer inlets, buffer outlets, and electrode access. A separate 645 µm hole was drilled using a diamond tipped bit at the top of the separation channel to create the sample inlet. The second wafer was then cleaned using Piranha solution before approximately 90 nm of amorphous silicon was deposited on the surface using plasma enhanced chemical vapor deposition. The two wafers were then aligned in a SB-6 Bonder and placed under 900 V for 2 h at 450 °C and 5 µbar. The device was then cut into a rectangle using a dicing saw with at least 1.5 cm between the edge and access holes. PEEK nanoports (IDEX Health and Science, Oak Harbor, WA) were attached to the access holes using epoxy rings. Silver conductive epoxy was used to seal the electrode access holes and attach wires to the electrodes. A 0.1 M NaOH rinse was performed for 150 min to remove any remaining amorphous silicon.

For both glass and ABS devices, Tefzel tubing (1/16” o.d. × 0.040 in i.d., IDEX Health and Science), PEEK knurl fittings (1/16” o.d. tubing, IDEX Health and Science),

and ETFE ferrules (0.063” hole, 1/16” o.d. tubing, IDEX Health and Science) were used to interface with the buffer inlets and outlets. Buffer was pumped through the buffer inlets using a syringe pump at 1.0 mL/min (Model #55-2222, Harvard Apparatus, Holliston, MA). Sample was pumped into the device through the sample inlet capillary using a syringe pump at 0.3 µL/min (Model #70-2213 Pico Plus, Harvard Apparatus), interfacing with the capillary via a zero dead volume connector.

Data Collection and Processing

LIF detection was performed using a 30 mW beam from a 150 mW diode pumped 488 nm solid state laser (Sapphire, Coherent, Santa Clara, CA). LIF detection was performed in a light tight enclosure using an AZ 100 stereomicroscope (Nikon Corporation, Tokyo, Japan) fitted with a 1.6× objective in conjunction with a Cascade 512B CCD camera (Photometrics, Tucson, AZ) and a 0.7× CCD lens. The microscope contained a filter cube with two bandpass filters from 450-490 nm and 500-550 nm as well as a dichroic mirror with a 495 nm cutoff. Images were collected at a rate of 5 Hz. Optimal camera settings for the glass device were 1× gain with an em gain of 0 for side-on alignment and 1× gain with an em gain of 3440 for the top-down alignment. Optimal camera settings for the ABS device were 2× gain with an em gain of 1000 for the ABS device in both alignments. Calibration curves were constructed with no voltage applied using fluorescein standards ranging from 0.1-0.5 µM, with fluorescein standards from 0.01-0.1 µM being necessary for the side-on alignment in the glass device. Line scans of each concentration were collected, exported as text files, and processed in Excel. All line scans were background subtracted using a signal recorded at each pixel across the device and averaged over three line scans prior to sample introduction into the device. LOD was calculated using the following equation:

$$LOD = \frac{3s}{m} \quad (2.1)$$

Where s is the standard deviation of the blank, and m is the slope of the standard curve.

Side-on Laser Alignment

For the side on LIF alignment (Figure 2.2) the laser is expanded by passing it through a 10× beam expander (Edmund Optics, Barrington, NJ). The beam is then focused to a point at the far side of the µFFE device using a 1-inch diameter planoconvex focusing lens with an effective focal length (EFL) of 100 mm (Newport, Andover, MA). With this alignment there is a slight increase in the power density of the laser as it focuses across the device, which could result in slightly better sensitivity for analytes on the far side of the separation channel.

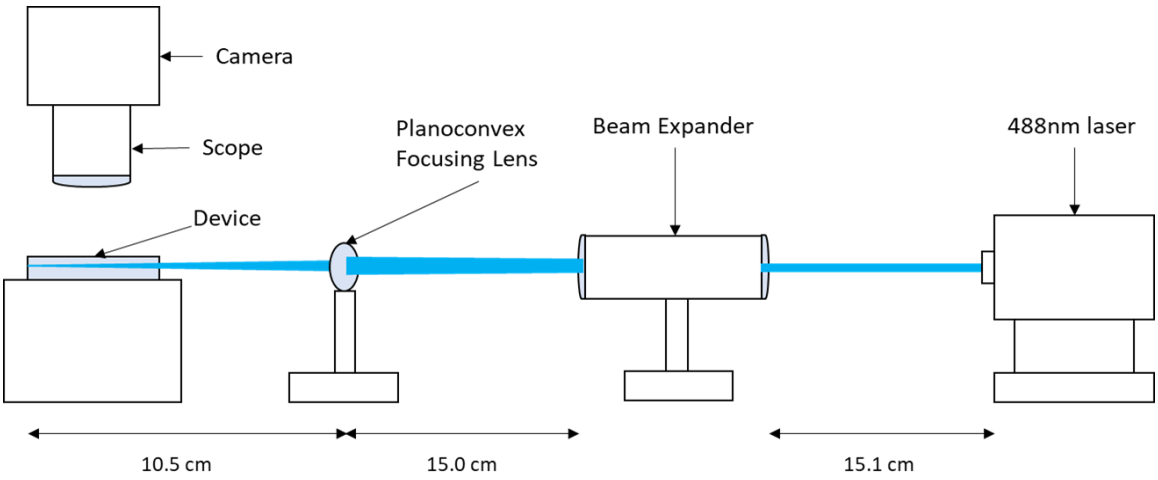

Figure 2.2 Schematic (not to scale) of the detection set-up used for side-on LIF analysis. The laser is first passed through a beam expander and then a focusing lens to focus the laser on the far side of the device. Distance given are approximate.

Top-down Laser Alignment

For the top down LIF (Figure 2.3) setup the laser first passes through a 50.8 × 20.4 mm planoconvex lens with an EFL of 100 mm (Newport) to collimate the laser into a horizontal line. The laser then passes through a 25.4 × 6.35 mm planoconcave cylindrical lens with an EFL of -6.4 mm (Newport) expanding the laser line. The laser

line is vertically collimated by passing it through a 50.8 × 50.8 mm planoconvex lens with an EFL of 150 mm (Newport). The laser line lastly reflects off a 1-inch diameter aluminum metallic mirror (Newport) at approximately 45° down onto the device resulting in a 2.5 cm wide and ~150 µm thick line across the device. Notably, in this alignment, there is a gaussian distribution of the laser power density as it is spread across the device, which is mitigated by spreading the laser line wider than the detection area.

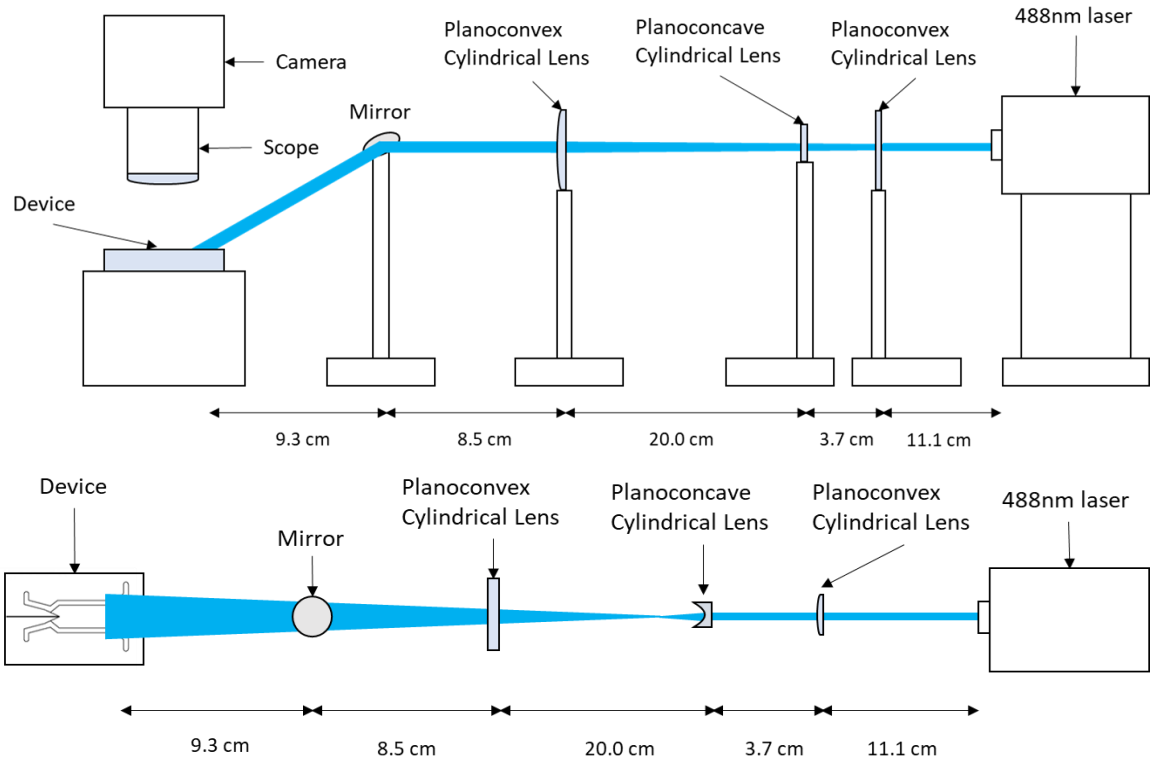

Figure 2.3 Side view (top) and top view (bottom) schematic (not to scale) of the detection set-up used for Top-Down LIF analysis. The laser is first collimated horizontally using a planoconvex cylindrical lens, then spread into a line using a planoconcave cylindrical lens. A second planoconvex cylindrical lens collimates the light vertically before the laser is reflected onto the device at an approximately 45° angle using a mirror. Distances given are approximate.

Results and Discussion

The goal of this experiment was to determine if LIF detection in µFFE could be improved by altering the alignment to bring the laser in directly through the side of the device, rather than spreading the laser into a line and reflecting it down onto it. The

impact of this new alignment was assessed by creating standard curves for fluorescein in both alignments for a glass and 3D printed ABS device. It is important to note that the separation channel height for the ABS device is approximately 4× greater than in the glass device. The devices also have different means of introducing the analyte into the device which results in differences in the stream width. The glass device introduces the sample into the separation channel using a 20 µm i.d. capillary through a 645 µm diameter hole on the face of the device. In the ABS device sample is introduced directly to the separation channel through a 20 µm i.d. capillary bonded into the side of the device. Consequently, only the relative improvement in sensitivity and LOD will be considered important. Furthermore, as no voltage was applied across the separation channel there is no hydrodynamic broadening of the fluorescein stream, and the LOD is not comparable to other reported results.

Glass Device

The glass device in both top-down and side-on laser alignment had a strong linear correlation between fluorescence and fluorescein concentration (Figures 2.5 and

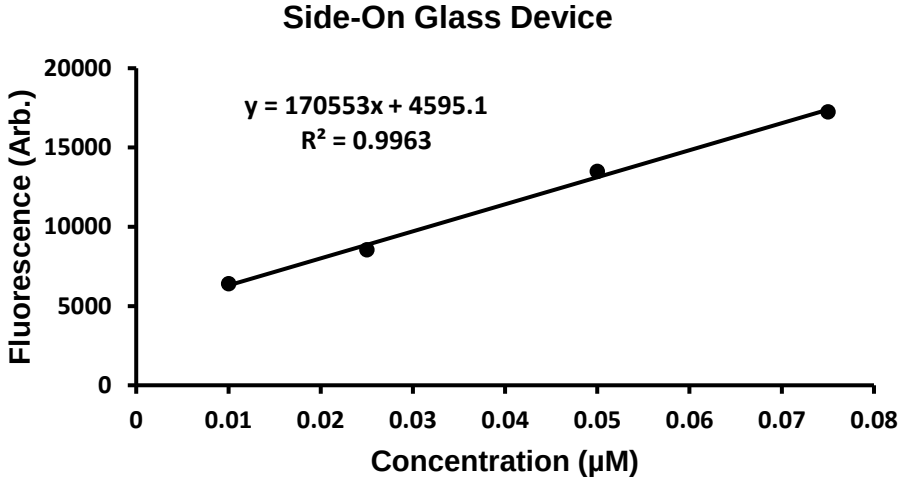

Figure 2.4 Standard curve for fluorescein on a glass device using side-on laser alignment. The results for the 0.1 µM were not included as photobleaching occurred due to the sample being left out overnight.

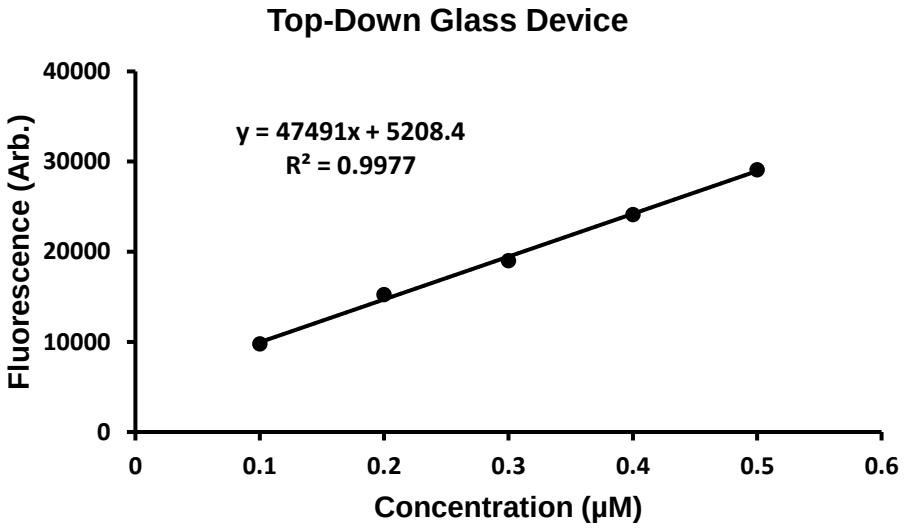

Figure 2.5 Standard curve for fluorescein on a glass device using top-down laser alignment.

2.6), with an R^2 of 0.9977 and 0.9963 respectively. Despite the side-on alignment using lower gain settings on the CCD it had 3-4× greater sensitivity (170553 μM^{-1}) than the top-down alignment (47491 μM^{-1}), necessitating the use of lower concentration standards to avoid maxing out the detector. An example of the line scan data for both alignments can be seen in Figure 2.6. The standard deviation within the blank for the

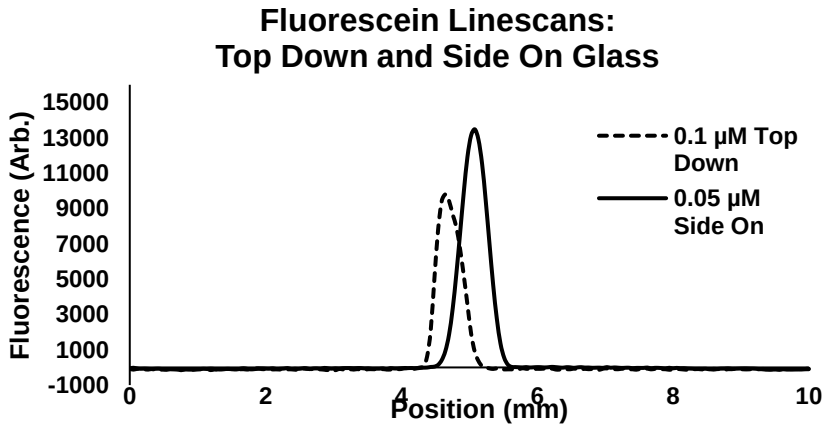

Figure 2.6 Line scans on a glass μFFE device of 0.1 μM fluorescein in top-down laser alignment and 0.05 μM fluorescein in side-on alignment. Despite having half the fluorescein concentration, the peak is approximately 37% larger.

top-down and side-on alignments were found to be 20.3 and 28.7 units, respectively. Using this data with equation 2.1 the LOD for fluorescein in the top-down laser alignment

was calculated to be 1.3 nM. Meanwhile, the LOD for the side-on alignment was calculated to be 0.5 nM. While this difference is significant, it is likely that the fluorophores are oversaturated in the side-on alignment. Further improvements could be made by reducing and optimizing the laser power, which would decrease noise while maintaining high sensitivity.

ABS Device

In top-down laser alignment, the ABS device had decent linearity between fluorescence and fluorescein concentration, with an R^2 value of 0.9825. In addition, the ABS device had good sensitivity in this alignment, with a slope of 99,517 μM^{-1}. Despite the high sensitivity, the rough surface of the ABS device in combination with the higher gain on the CCD led to substantially more noise than the glass device, with a blank standard deviation of 65.3 units. Using equation 2.1 the LOD for top-down laser alignment was calculated to be 2.0 nM for the ABS device.

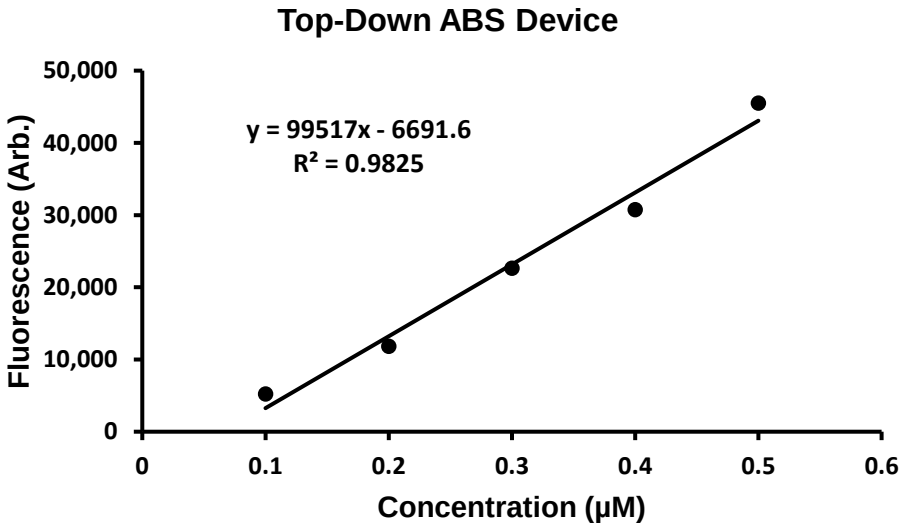

Figure 2.7 Standard curve for fluorescein on a 3D printed ABS device using top-down laser alignment.

No standard curve was collected for the side-on laser alignment in the ABS device due to the massive amount of laser light scattered presenting a significant hazard

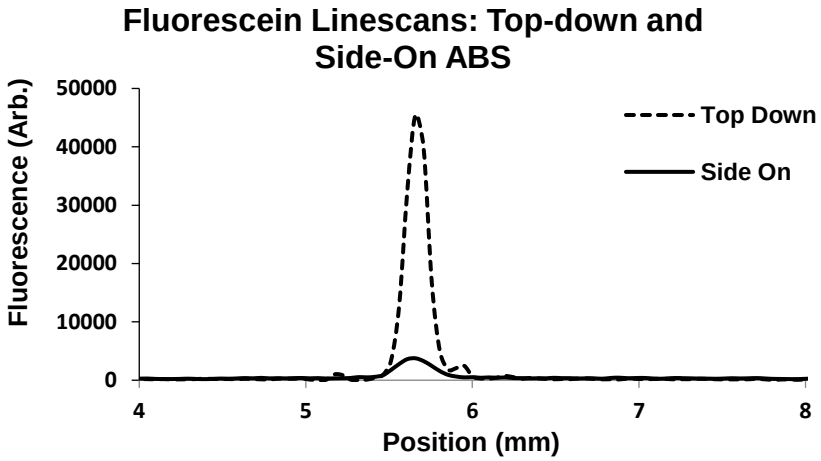

Figure 2.8 Line scans on an ABS µFFE device of 0.5 µM fluorescein in both side-on and top-down laser alignment. The sample flow rate for the side-on alignment was 1.5 µL/min, six-fold greater than in top-down alignment. Despite this the side-on peak is approximately 1/10th the height of the top-down peak.

to the operator. Notably the whole device was lit up by the laser light, illuminating the entire light tight enclosure. Due to the substantially increased background noise, excitation of the fluorescein was incredibly difficult, with the 0.5 µM sample requiring sixfold greater sample flow rate to produce a peak approximately one tenth the height of it's top-down peak (Figure 2.8). The intense light given off from the device could be a result of several factors such as the background fluorescence of the material and scattering of light through small gaps in the bond that arise due to print lines or semicrystalline regions that form due to stress caused by bonding conditions.

Table 2.1 LOD comparison for Fluorescein in top-down and side-on laser alignment for glass and ABS devices.

Device Material	Fluorescein LOD Top-down (nM)	Fluorescein LOD Side-on (nM)	Relative Improvement
Glass	1.3	0.5	62%
ABS	2.0	N/A	N/A

Conclusions

For a glass µFFE device, there is a substantial increase in sensitivity when utilizing side-on as opposed to top-down laser alignment for LIF detection. A roughly

62% improvement in the LOD for fluorescein was achieved when using side-on alignment. Despite the advantage, it should be noted that dicing a glass µFFE device to create the flat surface needed for side-on LIF creates a risk of breaking it. Due to the laborious and often expensive nature of glass µFFE fabrication, this should only be done if the improved sensitivity is necessary for the desired application.

No results were obtained for the 3D printed ABS devices due to intense scattering of the laser by the device making it clear that it is not compatible with side-on alignment. Future work should focus on improving side-on detection alignment through optimizing laser power and polishing the side of the devices to mitigate scattering as the laser enters. Furthermore, future µFFE devices should take the advantages side-on laser alignment into consideration when deciding what material and fabrication methods to use.

Chapter 3

On-line Buffer Exchange Micro Free Flow Electrophoresis Device Designs for the Development of Multi-Attribute Characterization Methods for Therapeutic Monoclonal Antibodies

Summary

Since it was first demonstrated by Chartogne et al. in 2000[13], the capability of micro free flow electrophoresis (μFFE) to perform on-line buffer exchange has seen no development despite significant advances in the field of μFFE. On-line buffer exchange enables efficient interfacing of traditionally incompatible separation techniques, such as isoelectric focusing (IEF) and electrospray ionization mass spectrometry (ESI-MS). The ability to interface such techniques directly and efficiently would allow significant improvements in the analysis of complex biological mixtures and compounds. In particular, on-line buffer exchange would allow for the development of new multi-attribute analysis methods for therapeutic monoclonal antibodies (mAb) that could significantly reduce the analytical workload required for quality assurance of the product.

This chapter will focus on the development of new μFFE device designs specifically for performing buffer exchange with therapeutic mAb's as the target analyte. Initially, a proof-of-concept design was 3D printed in acrylonitrile butadiene styrene (ABS). The buffer exchange capabilities of the design were tested via a malachite green assay which revealed removal of phosphate from the separation channel. Further designs were evaluated using the multiphysics modeling software COMSOL with the intent of resolving foreseen issues with ESI-MS interfacing. Specifically, ways to reduce the dilution factor of the μFFE device and eliminate neutral surfactants from the sample that are incompatible with ESI-MS were explored.

Introduction

The market for therapeutic monoclonal antibodies (mAb) has grown massively over the past decade. As of 2017, there were 57 commercially available variants and over 100 billion dollars in sales, with significant growth expected over the next decade.[105]

In contrast to traditional drug substances, monoclonal antibodies are produced using biological vectors, typically modified Chinese hamster ovary cells or myeloma cells, and exist as a mixture of highly similar compounds. The mixture arises due to differences in the epigenetic modifications of the protein sequence within the cells in a batch. With these epigenetic modifications being highly sensitive to production conditions batch to batch variation in the mixture composition must be considered.[106] These changes in the mixture can have significant impacts on the safety of the drug due to the possibility for an adverse immune response. Consequently, substantial quality assurance is needed for each batch to ensure the product is safe and functionally the same as the approved mAb. To this end a wide variety of analytical methods are used to characterize each batch including reversed phase high performance liquid chromatography (RP-HPLC), LC coupled with MS, size exclusion chromatography (SEC), affinity chromatography (AC), and a wide range of ion affinity chromatography (IAC) techniques.[107–109]

With so many techniques used for characterizing mAb's, recent work has sought to develop multi-attribute methods of analysis to reduce the analytical workload associated with their quality assurance.[110] This is done in large part through increased use of MS techniques due to their high accuracy and ability to detect the presence and, with certain techniques, the location of post-translational modifications.[107] To this end, the on-line interfacing of IAC and CE techniques with MS should be explored as a potential means of multi-attribute analysis of mAb's. To accomplish this, a means of rapid on-line buffer exchange is necessary to avoid ion suppression and remixing, which µFFE is well suited for.

The capacity of µFFE to perform online buffer exchange was first explored by Chartogne et al.[13] In their work, the authors utilized µFFE to remove ampholytes from a

capillary isoelectric focusing (cIEF) sample to allow on-line interfacing with ESI-MS. The combination of CIEF and ESI-MS is particularly valuable for protein characterization due to the high speed and accuracy at which the technique can analyze a complex mixture of proteins relative to the manually intensive two-dimensional gel electrophoresis methods traditionally used. The complication in interfacing cIEF and ESI-MS arises from the low volatility of the ampholyte salts in cIEF to generate the pH gradient that focuses the proteins based on their isoelectric point. High concentrations of ampholytes during cIEF results in good resolution and sample stacking, however the ampholyte ions suppress ionization of the protein during ESI, resulting in lower sensitivity. Conversely, if lower ampholyte concentrations are used, there is less suppression of the protein ion intensity in ESI-MS, but poorer resolution and sample stacking in cIEF.[60] Furthermore, higher concentrations of ampholytes have been shown to cause electrospray instability and salt deposition on the ESI-MS interface that can damage the instrumentation[61]. With its ability to continuously process sample, µFFE fits naturally as an intermediary between these steps as a means of exchanging the non-volatile ampholytes with a volatile buffer that is well suited for ESI-MS analysis. However, the difficulty in interfacing µFFE with ESI-MS and the additional sample dilution introduced by µFFE have led to µFFE being underdeveloped as a tool for on-line buffer exchange.

Since Chartogne et al. first demonstrated µFFE's ability to perform on-line buffer exchange several significant advancements have been made in the field of µFFE. Most notably, the efficient interfacing between multiple outlets on a µFFE device and ESI-MS[29]. Consequently, further work developing the capability of µFFE as a means of rapid on-line buffer exchange should be performed with the intent of interfacing traditionally incompatible separation techniques. This chapter will focus on developing an improved µFFE design for interfacing separation modes containing high concentrations of non-

volatile salt with ESI-MS. Specifically with intended use in multi-attribute methods of characterization and quality assurance for therapeutic monoclonal antibodies.

Theory

μFFE's ability to perform rapid online buffer exchange can be explained and modeled using three equations. First, an analyte stream position can be predicted using the following equation[1,2,7]:

$$d = \frac{EL\mu_{total}}{v} \tag{3.1}$$

Where E is the applied potential, v is the linear velocity of the separation buffer, and L is the analyte distance down the separation channel. μ_{total} is the total mobility of the analyte, which assuming no electroosmotic flow in the device would be equal to the electrophoretic mobility (μ_{ep}) of the analyte.

Second, assuming the use of a μFFE device with an open channel design and well matched conductivity between the sample and running buffer the stream width can be predicted using[2]:

$$\sigma^2_{total} = \frac{w^2_{inj}}{12} + \frac{2DL}{v} + \frac{h^2 d^2 v}{105DL} \tag{3.2}$$

Where σ^2_{total} is the overall peak variance, w_{inj} is the injection width of the sample stream, D is the diffusion coefficient of the analyte, L is the analyte distance down the separation channel, v is the linear velocity of the buffer in the channel, h is the height of the separation channel, and d is the deflection distance of the analyte.

Finally, since μ_{ep} values are not commonly available for many analytes, they can be approximated using the following equation:

$$\mu_{ep} = \frac{z}{6\pi\eta r} \tag{3.3}$$

Where z is the analyte charge, η is the viscosity, and r is the hydrodynamic radius of the analyte. Combined these equations can be used to create a simplistic model for buffer exchange on a µFFE device, which shows that separating small molecule buffers from an analyte with little or no μ_{ep} is trivial (Figure 3.1).

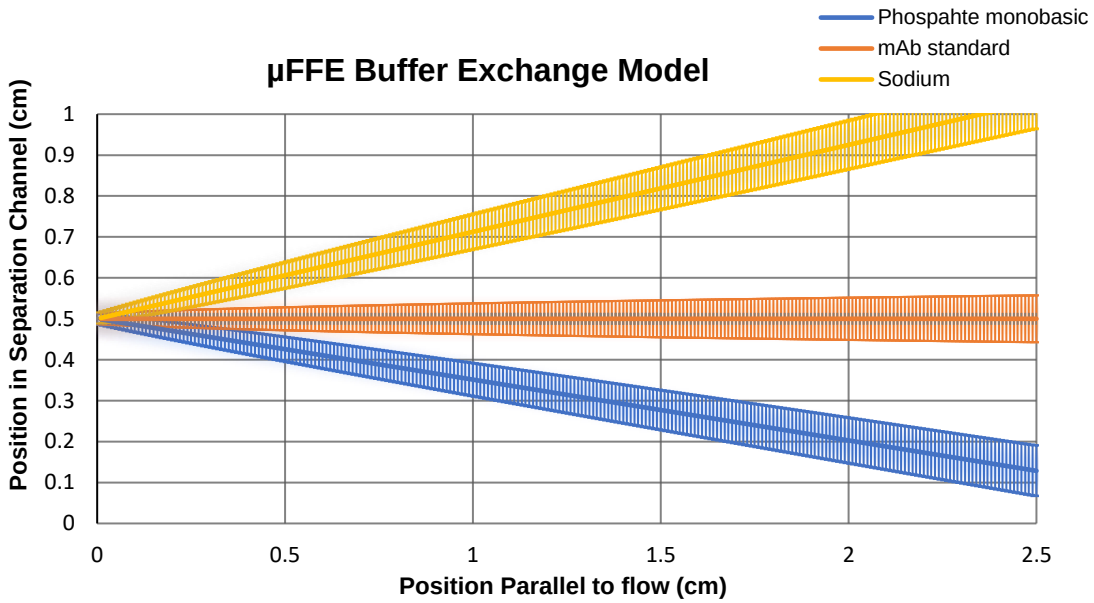

Figure 3.1 Modeled example of a buffer exchange using a theoretical mAb at its isoelectric point in a sodium phosphate buffer at an electric field strength of 75 V/cm. The electrophoretic mobility of phosphate monobasic was calculated at pH 7.0 using equation 3.3. The error bars are calculated using equation 3.2 and represent the stream width. The model neglects to show phosphate dibasic due to it having greater electrophoretic mobility than phosphate monobasic.

This model makes several assumptions: that there is no electroosmotic flow, that the separation buffer will immediately overpower the buffer in the sample stream, and that conductivity is well matched between the sample and running buffer. Many of these assumptions hold true for a typical µFFE separation, with EOF being suppressed via surface treatment if it is significantly present. In the case of using µFFE to perform a buffer exchange between IAC and ESI-MS, for example, the conductivity of the sample stream and running buffer are unlikely to be well matched. This mismatch in conductivity

introduces electrohydrodynamic broadening which is unaccounted for in this model. In a buffer exchange the sample stream will almost always have higher conductivity than the running buffer, which will cause de-stacking and broadening as the analytes leave the sample stream[33]. Since the intended target for the buffer exchange is a protein at or near its isoelectric point, where the μ_{ep} is very low, this should be of no consequence as the analyte is easily separated from the sample buffer. Even under acidic conditions where a protein is highly charged a relatively small protein like myoglobin has a μ_{ep} of approximately $2x10^{-4}$ cm^2/Vs[111] which is less than half that of sodium, which has a μ_{ep} of $5.19x10^{-4}$ cm^2/Vs[112], making their separation simple.

Experimental

Buffers and Solutions

All solutions were prepared in deionized water (18.2 MΩ, Milli-Q, Bedford, MA). All buffer solutions were filtered through a 0.22 µm nitrocellulose membrane filter (Fischer Scientific, Fairlawn, NJ). A 10 mM ammonium acetate (Malinckrodt, Dublin, Ireland) solution with 300 µM Triton X-100 (Sigma-Aldrich, St. Louis, MO) adjusted to pH 5.0 was used as the separation buffer. A 50 mM sodium phosphate (Sigma-Aldrich, St. Louis) solution with 300 µM Triton x-100 adjusted to pH 7.0 was used as the sample buffer. The color developing solution for the malachite green assay was produced by mixing a 0.2% (w/v) solution of malachite green (Santa Cruz Biotechnology, Dallas, TX) with a 4.2% (w/v) solution of ammonium molybdate (Santa Cruz Biotechnology, Dallas) in 4.5 M hydrochloric acid (Macron Chemicals, Center Valley, PA), and was filtered through a cellulose acetate syringe filter (0.45 µm, Restek, Bellefonte, PA) 30 minutes after mixing. 1.5% (w/v) tween 20 (Bio-Rad Laboratories, Hercules, CA) was used as the color preserving solution for the malachite green assay. A 0.5 mg/mL phosphate

stock solution was prepared using dried potassium phosphate (J.T. Baker, Randor, PA). A 0.5 µM fluorescein (Sigma-Aldrich, St. Louis) in sample buffer was used to visualize flow within the device.

Device Fabrication and Operation

ABS devices were fabricated based on work done by Anciaux et al.[6] The device was designed in two halves in Autodesk Inventor. The top half featured threaded fluidic connection ports for the buffer inlets and outlets. The bottom featured an 80 µm deep, 2.5 cm long, and 0.5 cm wide separation channel, a 345 µm deep electrode channel on both sides of the separation channel, and a 2 cm long, 300 µm wide, and 150 µm deep sample channel at the top of the separation channel. Both halves were printed simultaneously on an Ultimaker[2] fused deposition modeling (FDM) 3D printer with a 0.4 mm diameter nozzle. The print was performed using the following conditions: 260 °C nozzle temperature, 90 °C printing bed temperature, 10 mm/s printing speed, 20 µm layer height, and 106% material flow rate. Devices were printed in 2.85 mm diameter Transparent Premium ABS filament (Matterhackers, Lake Forest, CA). Electrode holes were drilled at a 30° angle into the tops of the electrode channels using a 400 µm bit and drill press (Micro-Mark, Berkeley Heights, NJ). Two approximately 5 cm long 250 µm diameter platinum wires (Sigma Aldrich) were inserted through the electrode holes and were fixed to the bottom of the electrode channels by carefully melting them into the ABS using a soldering iron.

Device halves were sealed by solvent assisted bonding using acetone vapors to activate the polymer surface. Acetone vapor exposure was performed in a fume hood by heating acetone in a Pyrex beaker on a hot plate to 90 °C. Acetone is flammable and caution should be taken while heating it. The half containing the channels was

suspended in the acetone vapor feature side down, exposed for 1.5-2 min, and allowed to dry for 2-3 min prior to bonding. While the channel half dried, the fluidic access half of the device was suspended port side up in the acetone vapor port side up, exposed for approximately 1 min, and allowed to dry for approximately 1 min before bonding. After drying, the 30 cm long, 300 µm o.d., 20 µm i.d. capillary (Polymicro Technologies, Phoenix, AZ) was seated in the sample channel and the two halves were aligned. Bonding was performed by hand by lightly pressing the device halves together along the sides of the device. The electrode holes were then sealed using quickset epoxy. The device was left to dry overnight at room temperature prior to use. Small copper alligator clips and lead wires were used to make electrical connections with the electrodes. After the devices were filled with fluid, they were stored with water in the channels to prevent the surface from drying out.

Tefzel tubing (1/16” o.d. × 0.040” i.d., IDEX Health and Science, Oak Harbor, WA) and PEEK fittings (1/16” o.d. tubing, IDEX Health and Science) and ETFE ferrules (0.063” hole, 1/16” tubing, IDEX Health and Science) were used to interface with the buffer inlets and outlets. Buffer was pumped through the buffer inlets using a syringe pump at 1.0 mL/min (Model #55-2222, Harvard Apparatus, Holliston, MA). Sample was pumped into the device through the sample inlet capillary using a syringe pump at 0.3 µL/min (Model #70-2213 Pico Plus, Harvard Apparatus), interfacing with the capillary via a zero dead volume connector. During operation, the left electrode was held at ground while 25-125 V was applied to the right electrode using a power supply (PS310, Stanford Research Systems Inc., Sunnyvale, CA).

Data Collection and Processing

Laser-induced fluorescence (LIF) was performed using a 30 mW beam from a 150 mW diode pumped 488 nm solid state laser (Sapphire, Coherent, Santa Clara, CA), which was broadened into an ~2.5 cm wide by ~150 μm thick line across the separation channel directly under the detection setup. LIF detection was performed at 1× zoom using an AZ 100 stereomicroscope (Nikon Corporation, Tokyo, Japan) mounted with a Cascade 512B CCD camera (Photometrics, Tucson, AZ). The microscope was fitted with a filter cube that had a 470/40 nm excitation filter, 525/50 nm emission filter, and a 495 nm cutoff dichroic mirror. A 1.6× objective (Nikon Metrology NV, Leuven, Belgium) was used along with a 0.7× CCD lens for detection. Images were acquired at a rate of 5 Hz with a gain of 1600. The detection setup was enclosed in a light tight enclosure (Newport, Irving, CA) within a darkroom.

Phosphate detection was performed via fraction collection at the separation channel and anode outlet for 25, 50, 75, and 125 V. Fractions were analyzed via a malachite green assay with absorbance detection performed at 660nm using a BioTek Synergy 2 plate reader (Agilent Technologies, Santa Clara, CA). Phosphate standards ranging from 1.05-10.5 μM were created by serial dilution of the phosphate stock solution using the ammonium acetate running buffer. Deionized water and sample buffer were used as the negative and positive controls, respectively. Solutions were prepared in the 96 well plate by mixing 315 μL of color developing solution and 63 μL of the standard, fraction, or control solution. Immediately after color formation 12.6 μL of the color preserving solution was added.[113] Analysis was performed immediately after all wells were prepared to avoid any decay in the signal.

Results and Discussion

Malachite Green Assay

Fraction collection for the malachite green assay was performed on a 3D printed ABS device with two inlets, three outlets, and a 0.5 cm wide separation channel. The separation voltage was applied, and the flow was allowed to stabilize over one minute prior to fraction collection. For fraction collection the outlet tubing was removed from the waste container and the end of the tube was quickly rinsed with deionized water and dried with a kimwipe before effluent was allowed to flow into the sample tube. Stream positions were disrupted during fraction collection, which lasted no more than 15 seconds to prevent the disrupted stream position from affecting the sample. Once approximately 0.5 mL of sample was collected the outlet tubing was returned to the waste container, and the flow was allowed to stabilize over one minute before repeating the process for the next outlet.

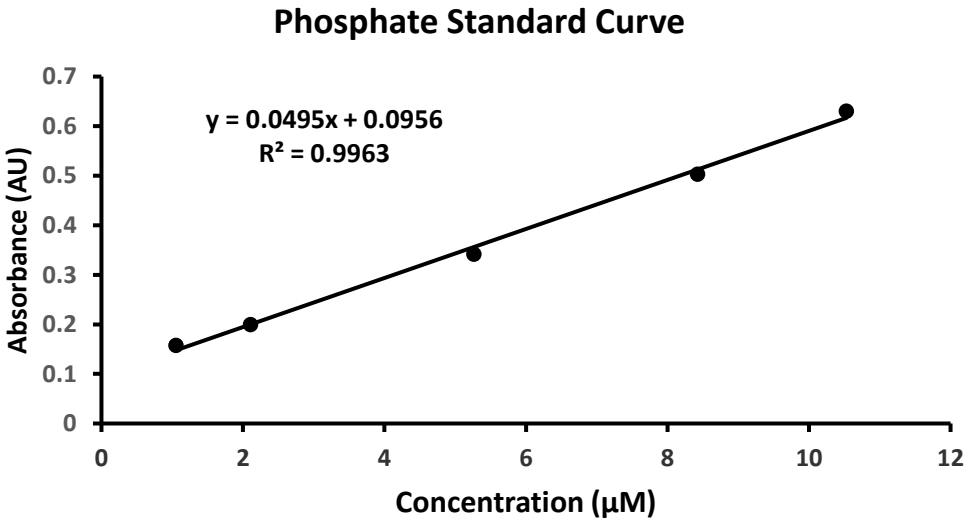

Figure 3.2 A Phosphate standard curve from 1.05-10.5 µM standards, measured using a malachite green assay at 660 nm.

Table 3.1 Phosphate concentrations in samples collected from the anodic and separation channel outlets at various voltages with a 95% confidence interval. Samples were assessed using a malachite green assay with their absorbance measured at 660 nm using a plate reader.

Voltage Applied (V)	Anode Phosphate Concentration (µM)	Separation channel Phosphate Concentration (µM)
25	0.5 ± 0.7	9.6 ± 0.7
50	0.7 ± 0.7	7.8 ± 0.7
75	4.1 ± 0.6	0.5 ± 0.7
125	2.8 ± 0.7	1.6 ± 0.7

The standard curve for phosphate obtained using this method shows strong linearity, with an R^2 value of 0.9963, and a limit of detection of 0.86 µM. The results from the separation channel show that the phosphate concentration in the separation channel at 75 V falls below the limit of detection, however due to the large confidence interval this is not certain. Increasing the voltage resulted in an increase in phosphate concentration in the separation channel due to the accumulation of electrolysis products . This was confirmed by whole chip imaging at 125 V using 0.5 µM fluorescein as the sample, which shows bubble accumulation in the electrode channel, and the fluorescein stream pulling back into the separation channel as it diverges from the electrode channel (Figure 3.3).

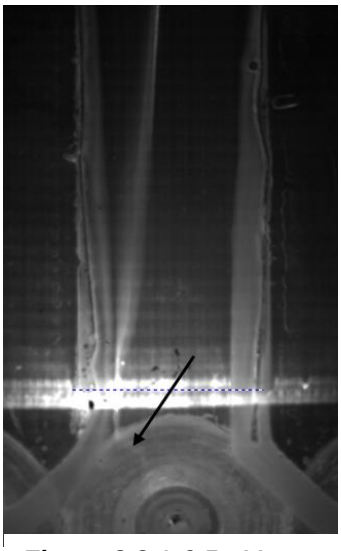

Figure 3.3 A 0.5 µM fluorescein sample with 100 V applied. The arrow points the fluorescein stream as it pulls back into the separation channel prior to exiting the device.

While more replicates at 75 V could be collected to improve confidence of the complete removal of phosphate from the separation channel, there are clear flaws in the design that need to be addressed. Notably, the single outlet in the separation channel requires the sample buffer to be pulled into the electrode channel and will result in more sample dilution. Furthermore, the design struggles to efficiently clear electrolysis products at higher voltages,

which may be necessary in scenarios where the sample buffer has a lower electrophoretic mobility. To address this, multiphysics modeling was used to assess the flaws of the design and to optimize a design for rapid on-line buffer exchange that can be efficiently coupled to ESI-MS.

µFFE Device Modeling

Device modeling was performed in 2D with COMSOL version 5.3, using laminar flow in combination with the shallow channel approximation with the channel thickness set to the separation channel height. Previously drafted devices were constructed by forming a union between distinct channels constructed out of Bézier polygons using vertices translated from the computer-aided design (CAD) file of the device. All other designs were formed using the basic geometry functions available in the program. Inlets and outlets were simplified into wall segments that match the diameter the inlets and outlets would be in the physical µFFE device. The running buffer inlets were set to laminar inflow with a set entrance length of 40 cm for electrode channel entrances and a varied pressure depending on channel dimensions. Outlets were set to laminar outflow with a set pressure of 1.0 atm, a set exit length of 40 cm at the electrode channel outlets, and a varied outlet length at the separation channel outlets. Sample inlets were not included as they are expected to have negligible impact on the overall pressure and flow rate within the device.

To account for deeper electrode channels and make the model function as expected based on lubrication theory[5], the dynamic viscosity in the side channels was reduced based on the squared ratio of the electrode channel height over the separation channel height. The entrance pressure in each model was tuned to approximately match expected separation channel linear velocities at a total volumetric flow rate of 2.0

mL/min from previous experimental results.[5] Due to modeled devices having different designs, channel heights, and electrode channel height to separation channel height ratios the modeled conditions do not reflect a 2.0 mL/min volumetric flow rate, however the conditions are within normal operating ranges of the devices.

Previous Glass Device Design

Initial modeling was based off previous glass μFFE designs[23,27] and was done to ensure modeling results were consistent with previous experiments.[5] The modeled device had a channel height of 10 μm and an electrode channel height of 40 μm. To generate the desired linear velocity within the device, a pressure gradient from 9.5 atm at the inlets to 1 atm at the outlets was used. The exit length at the separation channel outlets was 40 cm, the same as for the electrode channels. Once fluid reaches the separation channel the pressure quickly drops evenly, as shown by the straight and evenly spaced contour lines in the pressure plot in Figure 3.4. This contour pattern means fluid flow will occur straight down the device and any changes in the trajectory of an analyte will be solely due to deflection in the electric field. Notably, the contour lines begin to bend and spacing becomes uneven towards the bottom of the device as fluid streams converge at the outlets. Due to the bending and the large gap right before the electrode and separation channels diverge (arrow in Figure 3.4), some streams near the edge of the separation channel should get pulled into the electrode channels.

The loss of analyte streams into the electrode channels can be problematic if fractionation or further downstream analysis is desired. While the analyte streams can be retained by reducing the separation power and thus the distance they are deflected, this reduces the available separation space and could cause the loss of resolution between analyte streams. In the case of an on-line buffer exchange with a low mobility

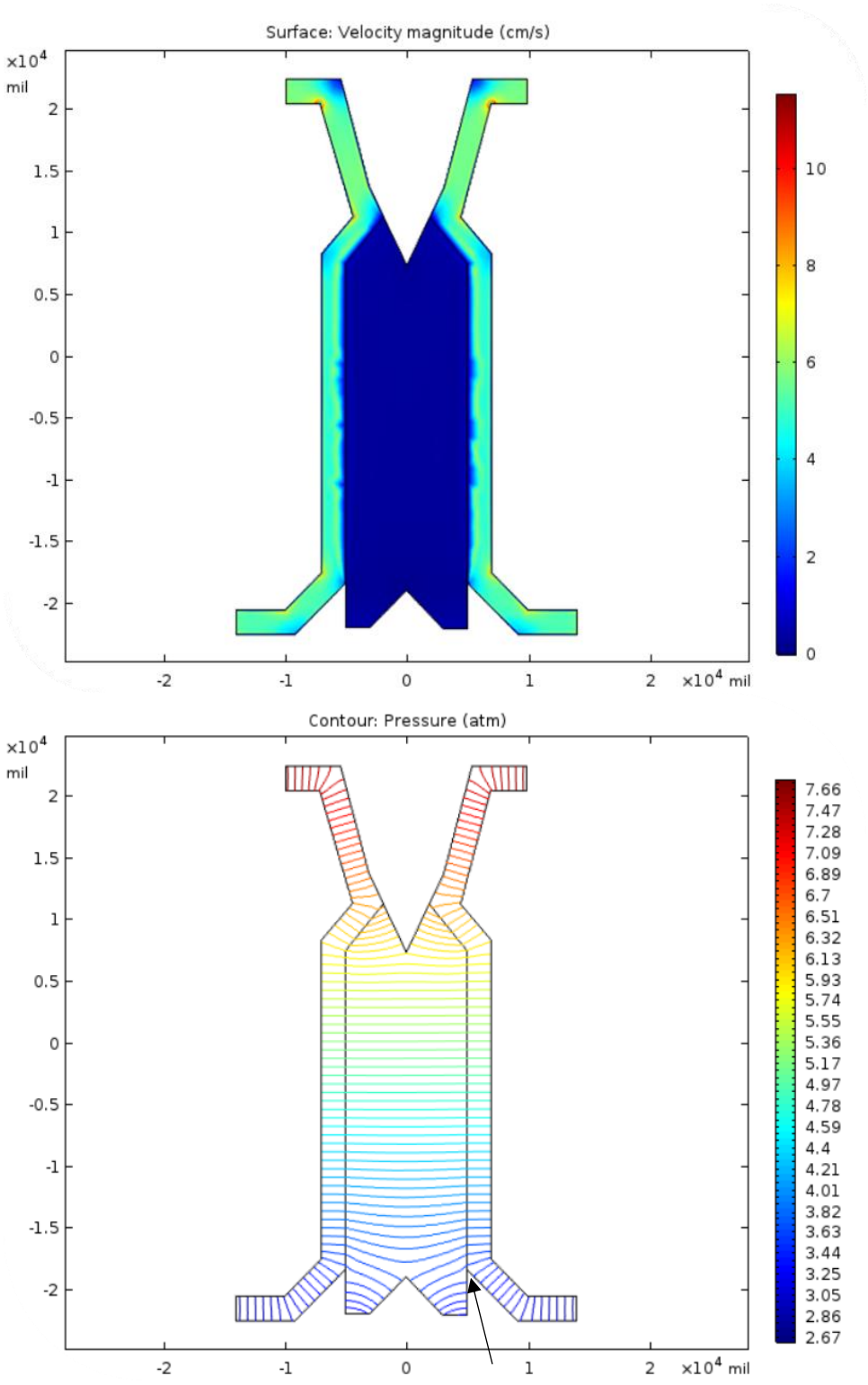

Figure 3.4 Velocity (top) and pressure (bottom) models for a two inlet four outlet µFFE device with a separation channel height of 10 µm and electrode channel height of 40 µm. The arrow points to where the electrode and separation channels diverge.

target analyte this could be used advantageously to aid in the complete removal of the sample buffer from the separation channel. However, this design does not address the need to remove neutral surfactants from the separation channel outlets or the complications that sample dilution could cause for downstream ESI-MS analysis.

Two Inlet Three Outlet Buffer Exchange design

The two inlet three outlet design was a proof-of-concept design created by altering the base glass design to have half the width and number of outlets in the separation channel, with the intent of pulling the sample buffer off into the electrode channels. The prototype device was fabricated in ABS using FDM 3D printing resulting in a separation channel height of 80 µm and electrode channel height of 320 µm. The increase in channel height drastically reduced the pressure gradient needed to generate the desired linear velocity, requiring only a drop from 1.05 atm at the inlets to 1 atm at the outlets. To balance the pressure across the separation channel, the separation channel exit length was reduced to 20 cm.

The resulting contours in Figure 3.5 show that pressure drops more rapidly at the separation channel outlet as opposed to the electrode channel outlets, which results in fluid in the electrode channel being pulled into the separation channel as the channels diverge. This is consistent with the phosphate assay results which showed that the effluent from the separation channel contained a substantial amount of the phosphate the separation was attempting to remove due to the accumulation of electrolysis products. To resolve this issue, more separation channel outlets are needed such that any fluid pulled back into the separation channel does not reintroduce the ions to the analyte.

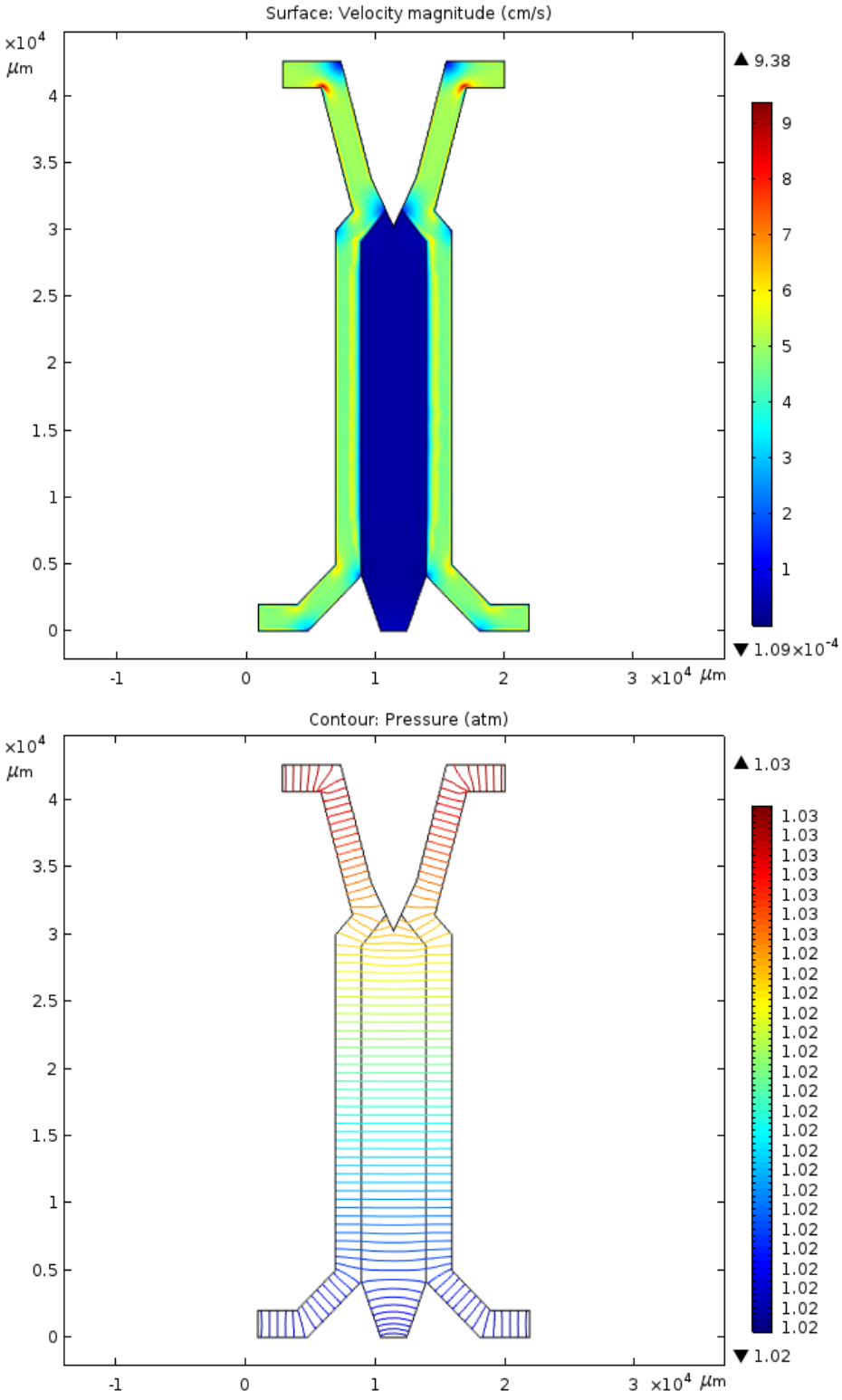

Figure 3.5 Velocity (top) and pressure (bottom) models for a two inlet three outlet µFFE device with a separation channel height of 80 µm and electrode channel height of 320 µm.

With regards to interfacing with ESI-MS, the two inlet, three outlet design does not address the need to remove neutral surfactants from the sample. Total removal of surfactant from the device is inadvisable as stream stability would greatly suffer due to inefficient removal of electrolysis products. Neutral surfactants capable of stabilizing flow in µFFE and compatible with electrospray could be explored or developed. This is not ideal, however, as some ionization suppression would still occur due to the presence of these surfactants.[114] Alternatively, the neutral surfactant could be segregated to the electrode channels by using additional buffer inlets that feed surfactant free buffer into the separation channel. With the diffusion coefficient for Triton x-100, a common neutral surfactant in µFFE, being 7.4×10^{-7} cm^2/s at lower concentrations[115] and residence time within the separation channel of the device being on the order of tens of seconds, there is no risk of surfactant making it past the outermost separation channel outlets of a device.

Four Inlet Five Outlet Buffer Exchange Design

The four inlet five outlet buffer exchange device design features two additional inlets, two additional outlets, and twice the separation channel width compared to the previous design. This design features depths of 28 µm and 200 µm for the separation and electrode channels, respectively. Flow was generated using a pressure gradient from 1.4 atm at the inlets to 1 atm at the outlets. To balance pressure across the separation channel the separation channel inlets entrance length was set to 15 cm and the separation channel outlets exit length was set to 24 cm. The pressure contours in Figure 3.6 show that the pressure drop in the separation channel outlets occurs faster than in the electrode channel outlet, meaning that some of the fluid from the electrode channels will likely pull into the outer separation channel outlets. The addition of two

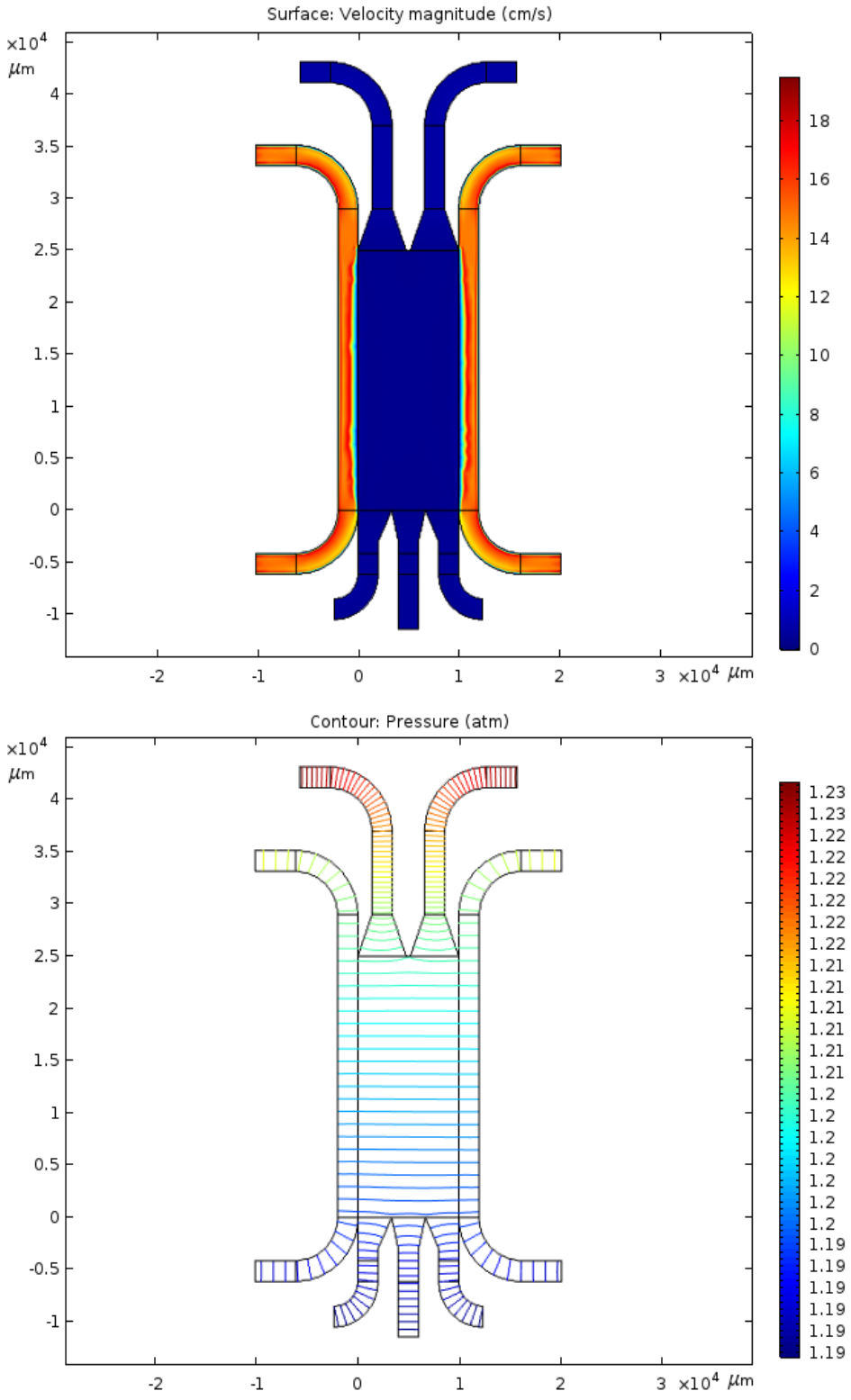

Figure 3.6 Velocity (top) and pressure (bottom) models for a four inlet five outlet µFFE device with a separation channel height of 28 µm and electrode channel height of 200 µm.

separation channel outlets, however, makes this inconsequential with a low mobility analyte that will exit through the centermost outlet.

The increased depth of the electrode channels relative to the separation channel resulted in an increased linear buffer velocity in the electrode channels. This will ideally result in more efficient removal of electrolysis products and allow stable flow with the application of larger voltages across the device. The addition of two additional inlets in the separation channel allows different buffers to be used in the separation channel and electrode channels. Specifically, using different buffers allows the use of surfactant free buffer in the separation channel to avoid ion suppression during ESI-MS detection. Meanwhile, surfactant containing buffer can be used in the electrode channels to aid in the efficient elimination of electrolysis products. The two added inlets also cause a distinct effect on flow that can be seen in the velocity profile of Figure 3.6 at the boundaries between the separation channel and electrode channels. The flow profile at the boundaries is curved in shape, seemingly being caused by fluid from the separation channel inlets pushing into the electrode channels as the channels meet and pulling back into the separation channel as they diverge. While the streams increase in speed as they pass into the deeper electrode channel, lubrication theory predicts that the linear velocity should be the same as the rest of the fluid in the electrode channel. This flow pattern is likely an artifact caused by modeling the device in 2D, similar to the small pockets of slower flow that can be seen in the velocity profile of Figure 3.4 at the separation and electrode channel boundaries.

Four Inlet Eight Outlet Design

The four inlet eight outlet design features a separation channel height of 28 μm and electrode channel height of 200 μm. Three more outlets were added to the

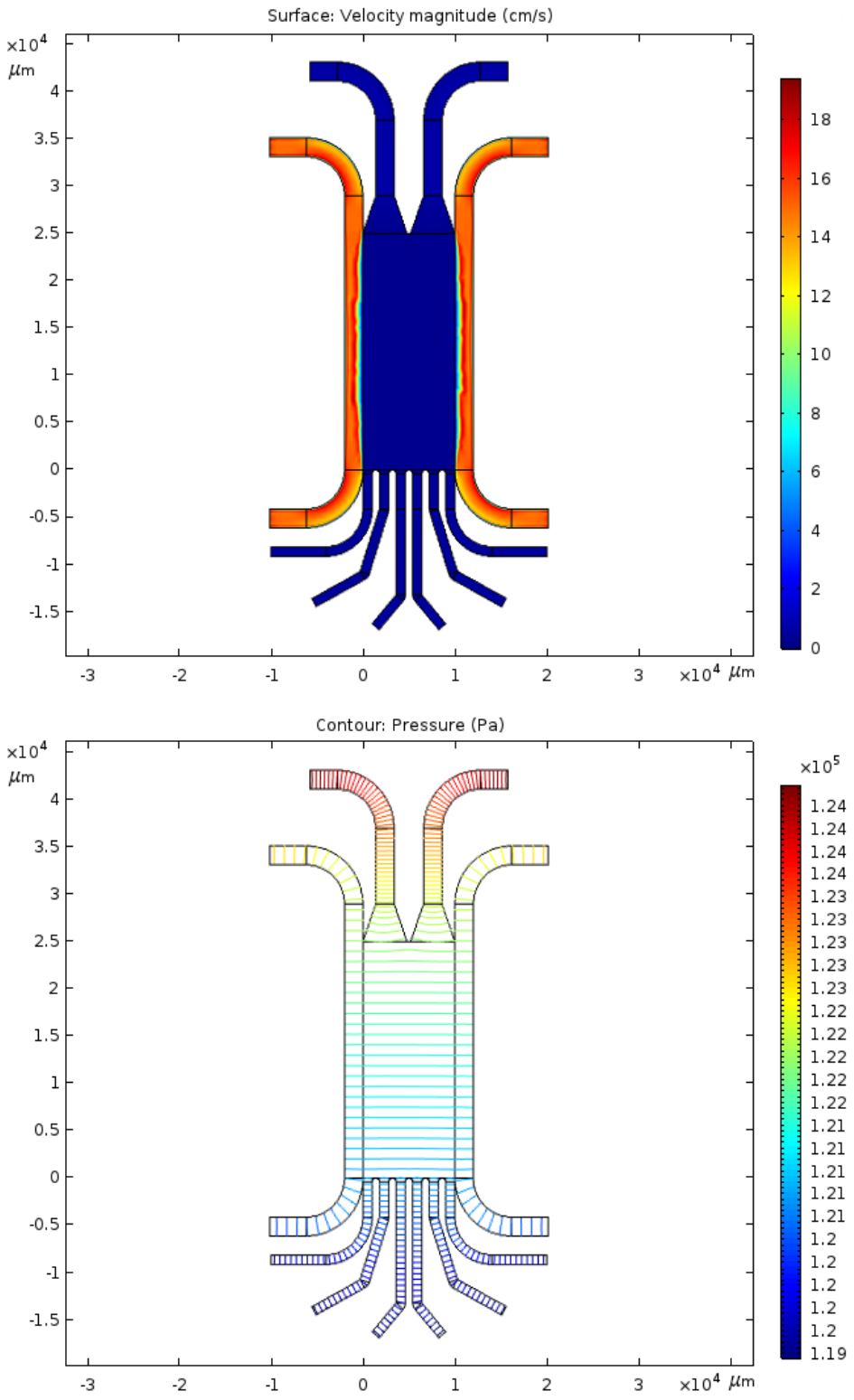

Figure 3.7 Velocity (top) and pressure (bottom) models for a four inlet eight outlet µFFE device with a separation channel height of 28 µm and electrode channel height of 200 µm.

separation channel relative to the previous design, and their widths were halved to accommodate them. Additional outlets were added to reduce the dilution factor of the sample if necessary and account for scenarios where multiple analytes need to be separated prior to downstream analysis. Flow was generated using a pressure gradient from 1.4 atm at the inlets to 1 atm at the outlets. To balance the pressure across the separation channel the separation channel inlets entrance length was set to 15 cm, and the separation channel outlets exit length was set to 20 cm. The pressure contour in Figure 3.7 shows that there is a significant increase in the pressure drop within the separation channel outlets, meaning that some fluid from the electrode channels will still pull into the outer separation channels. The velocity profile in Figure 3.7 also shows the same flow artifact as Figure 3.4 at the boundary of the separation and electrode channels.

Conclusion

Initial proof of concept experiments used an ABS 3D printed μFFE design with an open channel design, a narrow separation channel, and a single separation channel outlet. These experiments attempted to eliminate phosphate from the separation channel via deflecting it into the electrode channels. Phosphate concentration was monitored via a malachite green assay across multiple voltages which showed values dropping below the limit of detection with 75 V applied. Substantially higher voltages resulted in phosphate being reintroduced to the separation channel as electrolysis products accumulated. This was confirmed by fluorescence imaging of a fluorescein sample at 125 V (Figure 3.3). Multiphysics modeling using COMSOL (Figure 3.5) further revealed that the pressure balance at the outlets could cause fluid to draw back into the separation channel as it diverged from the electrode channel.

Further multiphysics modeling was performed using COMSOL to address future issues associated with interfacing μFFE with ESI-MS such as neutral surfactant exiting with the sample, and excessive dilution of the sample. Modeling revealed that balancing the pressure gradient down the separation channel in these open channel designs led to an imbalance in the pressure drop between the electrode channel outlets and the separation channel outlet. This imbalance leads to either fluid from the electrode channel spilling into the separation channel or vice versa. Newer designs that were modeled incorporated extra channels in the separation channel to catch the spill and prevent it from contaminating the sample stream that should theoretically exit out the centermost outlets. The incorporation of extra channels further served to minimize the dilution factor of the sample, with a design featuring as many as six outlets in the separation channel being reported. The new designs also incorporated two additional buffer inlets to feed surfactant free buffer into the separation channel to eliminate neutral surfactant from the sample. While some neutral surfactant is expected to diffuse from the electrode channels into the separation channel, the low residence times of solution in the separation channel, on the order of tens of seconds, results in insufficient time for it to diffuse into the center outlets of the separation channel.

Future work should attempt physical fabrication of these new designs to test how well the design changes impact their efficiency at online buffer exchange and capability for interfacing with ESI-MS. Specifically, the malachite green assay can be used to ensure the near complete removal of sample buffer from the analyte, while matrix assisted laser desorption/ionization time of flight mass spectrometry (MALDI-TOF) can be used to assess the presence and quantity of neutral surfactant in the sample stream based on relative ionization suppression in the sample without the risk of damaging electrospray instrumentation. Further work should also assess minimizing the applied

voltage to achieve complete or near complete removal of sample buffer with the intent of achieving the longest windows of stable operation possible.

Chapter 4

Fabricating μFFE devices in COC via Hot Embossing from a Poly-jet 3D Printed Master Mold

Summary

The fabrication of high-performance microscale devices in substrates with optimal material properties while keeping costs low and maintaining the flexibility to rapidly prototype new designs remains an ongoing challenge in the microfluidics field. To this end, we have fabricated a micro free flow electrophoresis (μFFE) device in cyclic olefin copolymer (COC) via hot embossing using a poly-jet 3D printed master mold. A room temperature cyclohexane vapor bath was used to clarify the device and facilitate solvent assisted thermal bonding to fully enclose the channels. Device profiling showed 55 μm deep channels with no detectable feature degradation due to solvent exposure. Baseline separation of a fluorescein, rhodamine 110, and rhodamine 123, was achieved at 150 V. Limits of detection for these fluorophores were 2 nM, 1 nM, and 10 nM, respectively, and were comparable to previously reported values for glass and 3D printed devices. Using poly-jet 3D printing in conjunction with hot embossing, the full design cycle, from initial design to production of fully functional COC μFFE devices, could be completed in as little as 6 days. By producing devices in parallel, several could be fabricated from an embossing mold in a single day.

Introduction

μFFE devices have been fabricated using a wide variety of methods, including wet etching[4,37], computer numeric control milling[72,116], injection molding[38], multistep liquid-phase lithography[36], and multi-step lamination[18,117]; in a broad range of materials including silicon[1], glass[4], poly(dimethyl siloxane) (PDMS)[66], poly(methyl methacrylate) (PMMA)[35], acrylonitrile butadiene styrene (ABS)[6], and cyclic olefin polymer (COP).[38] Each material presents its own advantages and disadvantages in terms of sensitivity, separation efficiency, chemical compatibility, and ease of fabrication. Glass, for example, is an optically transparent, rigid material that is stable over a wide range of pH,

while being relatively chemically inert. However, glass devices are relatively expensive and slow to produce, requiring a specialized fabrication facility for much of the process. Furthermore, glass μFFE devices often require frequent treatment to ensure consistent surface chemistry and prevent surface adsorption.[8]

In contrast, fabrication of microfluidic devices in PDMS is fast and inexpensive.[12,66,67] However, the elasticity of the material combined with the low aspect ratio of the separation channel in μFFE devices requires special design considerations such as posts that can decrease separation space and efficiency.[67] The hydrophobicity of PDMS creates additional challenges, making bubble-free filling by aqueous solvents difficult, and allowing hydrophobic analytes to readily adsorb to the surface. The hydrophobic surface also complicates the removal of bubbles that form at the electrodes of a μFFE device due to electrolysis, which can quickly accumulate and disrupt flow.[40] To avoid these issues the hydrophilicity of the surface can be modified using a variety of methods; however, PDMS can quickly recover its hydrophobicity due in part to its extremely low glass transition temperature.[69,70]

Rigid polymers like PMMA, ABS, COP, and cyclic olefin copolymer (COC) provide a compromise between glass and PDMS, being less expensive and faster to produce than glass devices with better performance characteristics than PDMS.[6,18,38,116] COC has seen increased usage as a material to produce microfluidic devices over the past decades due to its many desirable properties. In addition to being cheap and rigid, it has both high optical clarity and low background fluorescence, allowing highly efficient sample detection.[73] COC is also resistant to acids, bases, and most polar organic solvents such as acetone and methanol. COC boasts extremely low water absorption (<0.01%), an order of magnitude less than PMMA, which results in humidity having little

to no effect on reproducibility.[74] However, like many plastics, the surface of COC is hydrophobic, and like PDMS can require surface modification to be suitable for protein analysis.[118]

COC has several variations in microstructure, each with different thermal resistances and viscosities that can be selected based on the desired application.[119] Combined with its low density, this makes COC an excellent material for fabrication methods like injection molding and hot embossing, where the low viscosity improves fidelity. As a result, hot embossing and injection molding are the primary methods used for fabricating COC microfluidic devices.[73,74,120] Hot embossing provides better replication accuracy for microstructures, in addition to less shrinkage and warping compared to injection molding.[80] To our knowledge hot embossing has yet to be explored as an option for µFFE device fabrication.

Hot embossing is a process in which a polymer is heated above its glass transition temperature, and a mold is then pressed into it, imprinting features into the polymer. Master molds for this process are typically produced in silicon wafers using Deep Reactive Ion Etching (DRIE).[74] This technique is exceptional at producing high aspect ratio structures, but defects in the wafer and uneven etch rates make DRIE non-ideal for larger scale µFFE designs that cover several square centimeters.[121] Combined with the cost of operating and maintaining DRIE equipment, this method of mold fabrication is poorly suited for µFFE device development where quick iteration of designs is desired.

Poly jet 3D printing provides an excellent alternative to DRIE for the fabrication of larger mold designs. Poly jet 3D printing relies on jetting microdroplets of photocurable polymer from ink-jet style print heads followed by rapid curing with UV lamps attached to

the 3D print cartridge.[122] Poly jet 3D printing can produce layer heights as low as 14-28 µm. Combination with computer-aided design (CAD) software allows rapid iteration of new designs. 3D printing also provides easy control over the taper of the mold, which is particularly important for demolding when hot embossing.[123] With regards to µFFE, poly jet 3D printing provides a viable means of rapidly producing and iterating mold designs for hot embossing.

In this chapter we assess the potential of hot embossing to produce high performance, low cost, µFFE devices in COC. While other methods for cheap and rapid µFFE production exist, they are nor well suited for fabrication in COC or have the same potential for high-fidelity, high-throughput fabrication.[6,35,66] The use of a poly jet 3D printer will also be assessed as a means of producing hot embossing master molds to allow faster prototyping of COC devices without the need for expensive nanofabrication techniques or design testing in alternative materials.

Experimental

Materials and Solutions

Solutions were made with deionized water (18.3M, Milli-Q; Millipore, Bedford, MA) and filtered through a 0.22 µm nitrocellulose membrane (Millipore). µFFE separation buffer was 300 µM Triton X-100 (Sigma-Aldrich, St. Louis, MO) and 25 mM HEPES (Sigma-Aldrich) with the pH adjusted to 7.00. Fluorescent dye solutions consisted of fluorescein, rhodamine 110 chloride, and rhodamine 123 (Sigma-Aldrich) dissolved in separation buffer. Verowhite resin (Sculpteo Inc., Oakland, CA) was used to 3D print the master mold. Silastic RTV-3110 (Sigma-Aldrich) catalyzed by Xiameter RTV-3010S (Sigma-Aldrich) was used to cast a negative of the master mold. Weicon C (Weicon, Ontario, Canada) was used to make the embossing molds. Transparent

acrylonitrile-butadiene-styrene (ABS) (Matterhackers, Lake Forest, CA) was used to 3D print the bonding rigs. TOPAS 6017s-04 cyclic olefin copolymer (COC, 6 x 6 x .040" molded plates) was used to make the devices (TOPAS, Raunheim, Germany), and was cut to the desired size using a Universal Systems PLS6.150D Laser Cutter (Universal Laser Systems, Scottsdale, AZ). The electrodes for the COC devices were 100 µm diameter platinum wire (Sigma-Aldrich). Quickset Epoxy (Loctite, Westlake, OH) was used to secure ports and seal the electrodes into the device. Cyclohexane (Fisher Scientific, Hampton, NH) was used to make cyclohexane vapor for clarifying and bonding the COC halves. Crystal Bond (Electron Microscopy Sciences, Hatfield, PA) was used to seal the capillary in the COC devices.

COC µFFE Device Fabrication

Figure 4.1 shows an overview of the µFFE hot embossing fabrication process. The master mold was designed in Autodesk Inventor and printed on a Stratasys J750 Poly-jet 3D printer (University of Minnesota Medical Device Center). The CAD file was a negative of the final imprinted design and included a 28 µm tall × 2.5 cm long × 1 cm wide separation channel, as well as 200 µm tall electrode channels, and a 400 µm tall × 400 µm wide capillary inlet channel. The separation channel was smoothed using a wet sand with 1500 grit followed by 3000 grit sandpaper to remove print lines and reduce the channel height. The mold was cast in Xiameter RTV-3010S catalyzed Silastic RTV-3110 and allowed to cure overnight before careful separation. The Silastic mold was then cast in Weicon C polymer (Weicon, Ontario, Canada) and was backed with an aluminum block wrapped in heavy duty aluminum foil. After curing at room temperature for 48 hours, the block and foil were removed, and any excess polymer was chipped away. The mold was then tempered to withstand embossing conditions by heating on a hotplate at

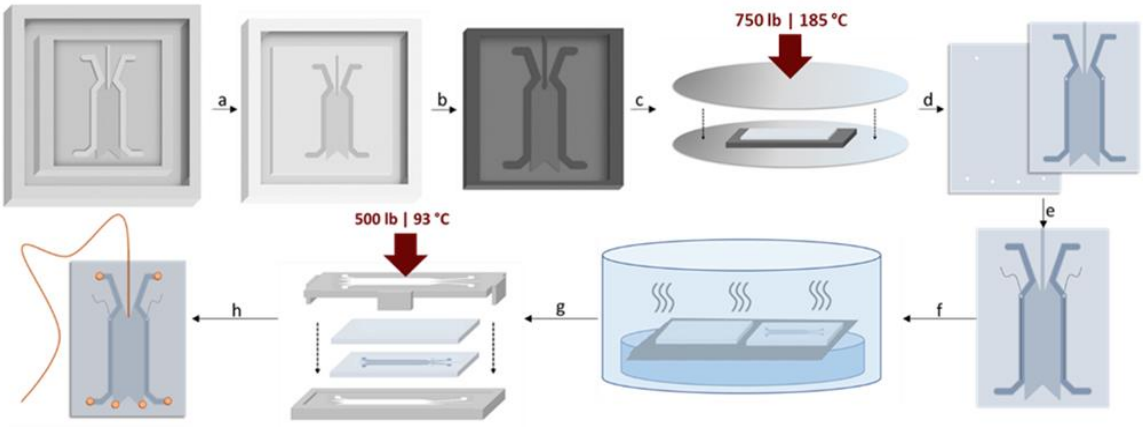

Figure 4.1 Schematic of µFFE device fabrication in COC using hot embossing. (a) Cast master mold in silicone. (b) Recast silicone mold in Weicon C. (c) Hot embossing. (d) Drill inlet, outlet, and electrode holes. (e) Attach electrodes. (f) Cyclohexane vapor exposure. (g) Bond under heat and pressure in bonding rig. (h) Attach buffer ports and sample capillary.

40-120°C over 18 hours, increasing the temperature by 20°C each hour until reaching 120°C.

Hot embossing was performed on a Carver thermal press with an embossing temperature of 185°C, a de-embossing temperature of 173°C, and a load of 750 lb. Prior to embossing, the COC polymer was cleaned with acetone to remove any residual compounds from the surface and dried using compressed air. The Weicon C mold was carefully aligned with a 5.8 cm x 4.5 cm x 1 mm thick piece of COC between two flat, mirror-polished, steel plates before being placed in the pre-heated thermal press. The mold and polymer were then allowed to reach thermal equilibrium at the embossing temperature (173 °C) over approximately 60 s before the load was slowly applied over 15s. The press was then cooled to the de-embossing temperature where the load was released, and the mold and imprinted polymer were separated.

Imprints were placed feature side down and propped approximately 1 mm off a wire mesh stage above a 150 mm petri dish filled with 100 mL of cyclohexane. This was then sealed using an inverted crystalizing dish, exposing the imprints to cyclohexane

vapors at room temperature for 28 min to smooth and clarify the imprinted COC wafers (Figure 4.2). The imprints were then allowed to dry completely.

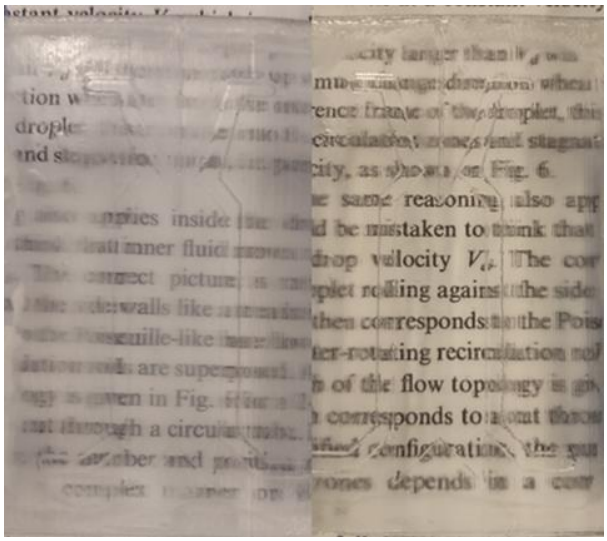

Figure 4.2 The clarity of an embossed COC wafer before (left) and after (right) 28 minutes of cyclohexane vapor exposure. Embossed wafers were held 1.6 cm above the text during imaging to showcase the difference in clarity.

Wire electrodes were inserted into 0.4 mm holes drilled at a 30° angle at the top of each electrode channel. These wires were then embedded in the electrode channels by carefully melting them into the COC with a soldering iron. A second 5.8 cm × 4.5 cm × 1 mm thick piece of COC had two 1 mm buffer inlet and four 1 mm buffer outlet holes drilled into it.

The surfaces of the two COC pieces were activated for bonding using cyclohexane vapor in the exposure chamber described above. The non-imprinted and imprinted halves were exposed face-down at room temperature for 40 and 12 min, respectively. The halves were then aligned in a 3D printed ABS bonding rig, placed into a Carver thermal press at 93°C, and put under a 500 lb load for 20 min, at which point the load was released and the bonded device was removed from the rig.

The electrode holes of the device were sealed using quickset epoxy. The PEEK nano-ports (Upchurch Scientific, Oak Harbor, WA) were applied to the buffer inlet and outlet ports using quickset epoxy. A 150 µm o.d., 20 µm i.d. fused silica capillary (Polymicro Technologies, Phoenix, AZ) was positioned in the capillary channel. Crystal bond was then melted at 125 °C on a hot plate and drawn into the capillary channel by vacuum. Electrical connections were fixed to the device using quickset epoxy, soldered to the exposed wires, and the wires were coated in epoxy to avoid accidental damage. An example of a fully assembled device can be seen in Figure 4.3.

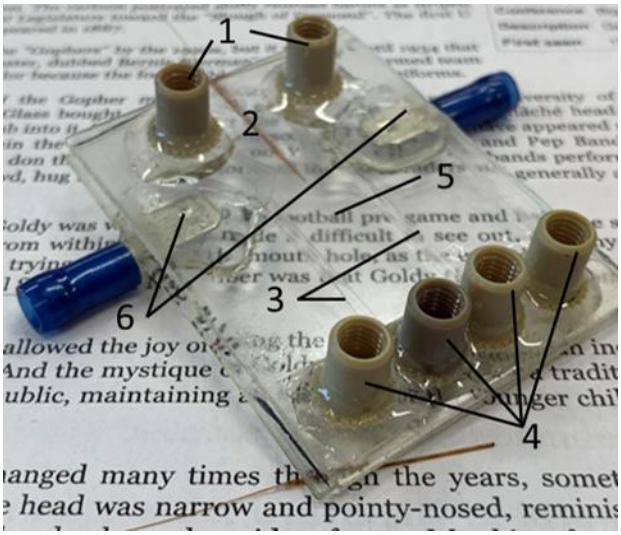

Figure 4.3 Image of a fully fabricated COC µFFE device. Labels show the (1) buffer inlets, (2) sample inlet, (3) electrodes and electrode channels, (4) buffer outlets, (5) separation channel, and (6) electrical connections.

µFFE Separations

Tefzel Tubing (1/16” o.d. × 0.040” i.d., IDEX Health and Science, Oak Harbor, WA) and PEEK fittings (1/16” o.d. tubing, IDEX Health and Science) and ETFE ferrules (0.063” hole, 1/16” o.d. tubing, IDEX Health and Science) were used to interface with the buffer inlets and outlets. Separation buffer was pumped into the device through the buffer inlets using a syringe pump at 0.5 mL/min per channel (Model #55-2222, Harvard Apparatus, Holliston, MA). A three-dye mixture was pumped into the device through the

sample inlet capillary using a syringe pump at 0.5 µL/min (Model #70-2213 Pico Plus, Harvard Apparatus), interfacing with the capillary via a zero dead volume connector. During separations, 0-150 V was applied to the left electrode using a power supply (Model PS310/1250V-25W, Stanford Research Systems, Sunnyvale, CA) and the right electrode was grounded.

Laser Induced Fluorescence Detection and Data Collection

Laser-induced fluorescence (LIF) was performed using a 30 mW beam from a 150 mW diode pumped 488 nm solid state laser (Sapphire, Coherent, Santa Clara, CA), which was broadened into an ~1.5 cm wide by ~150 µm thick line across the separation channel directly under the detection setup. LIF detection was performed at 1× zoom using an AZ 100 stereomicroscope (Nikon Corporation, Tokyo, Japan) mounted with a Cascade 512B CCD camera (Photometrics, Tucson, AZ). The microscope was fitted with a filter cube that had a 470/40 nm excitation filter, 525/50 nm emission filter, and a 495 nm cutoff dichroic mirror. A 0.5× objective (Nikon Metrology NV, Leuven, Belgium) was used along with a 0.7× CCD lens for detection. Images were acquired at a rate of 5 Hz with a gain of 1600. The detection setup was enclosed in a light tight enclosure (Newport, Irving, CA) within a darkroom. Line scans of samples and blanks were exported as a text file and processed using a custom MATLAB script.

µFFE Depth Profiling

The feature depths of hot embossed COC wafers were profiled before and after cyclohexane vapor exposure using a KLA-Tencor P7 surface profiler (KLA, Milpitas, CA) with a scanning speed of 100 µm/sec and a total scan distance of 15 mm. The imprints were flattened prior to profiling to ensure the P7 stage vacuum would hold them by heating them to 163 °C in a thermal press between two flat, mirror-polished, steel plates

under a load of 500 lbs. The press was cooled to 108 °C and the imprints were removed and allowed to cool to room temperature.

Results and Discussion

Our goal was to develop a fabrication method to produce high performance µFFE devices at low costs with while maintaining the potential for rapid prototyping and design iteration. Hot embossing was chosen as a fabrication approach that enabled production in COC, a highly desirable polymeric substrate with high clarity, broad chemical resistance, and low water absorption. Master molds were produced using 3D printing, allowing control over important features such as tapered edges and enabled rapid turnaround in the design cycle.

The overall design of the hot embossed COC µFFE devices were similar to those previously described by our group in glass and 3D printed device designs with one significant difference. In previous designs[5,6] the electrode channels were 4× deeper than the separation channel resulting in 16-fold higher linear velocity in the electrode channel in comparison to the separation channel. These deeper electrode channels efficiently eliminate electrolysis bubbles from the device, ensuring stable buffer flow[5]. With COC being more hydrophobic than glass, and therefore more likely to retain bubbles, the electrode channel was designed to be 10× deeper resulting in 100-fold faster linear velocity in the electrode channel than the separation channel.

Mold Optimization

Using a poly-jet 3D printed master mold presented unique benefits and limitations. In addition to being faster and cheaper than traditional mold fabrication methods, the use of 3D printing allows for rapid changes to the master mold design with significant control over the taper of feature edges. Insufficient taper causes the mold and

polymer to lock together during de-embossing, causing substantial damage and eventual failure of the Weicon C mold. A limitation of the poly-jet 3D printed master mold is the variance in the XY axis combined with the staircase pattern of the printed mold in the Z axis. As a result, the 3D prints have rough side walls which require larger tapers to overcome. Our initial designs used a 2° taper that led to mold failure within the first few hot embossing cycles. The taper was increased to 5° which allowed molds to last for roughly 15-30 cycles before naturally wearing down enough to warrant replacement. The use of such high tapers is of little consequence to our structure due to the low aspect ratio of the µFFE separation channel. However, large taper angles present a substantial limitation with regards to high aspect ratio structures, such as the narrow channels often used in microfluidic devices.[120,124] The other major limitation poly-jet 3D printing presents is the artifacts it creates in the form of print lines. These transfer through the process to the device and scatter light, reducing the device's performance. The separation channel of the master mold was sanded using 1500 and 3000 grit sandpaper until the print lines were no longer visible to minimize the effect of these artifacts.

Embossing Optimization

The embossing and de-embossing temperatures tested were kept within 5-15°C of the COC's glass transition temperature (178 °C). This range of temperatures was used to reduce thermally induced stress caused by the difference in thermal expansion coefficients between the COC polymer and Weicon C mold.[124] The optimal conditions for the embossing cycle were judged based on several easily observable qualitative factors including COC polymer warping, poor filling around features, Weicon C mold damage, and COC polymer sticking to the Weicon C mold. Poor filling around the mold structures was an indication that the embossing temperature was too low, preventing sufficient COC polymer flow during embossing. Warping of the substrate indicated that

the embossing temperature was too high, causing the COC to flow too readily and distort its shape. COC polymer sticking to the mold demonstrated that the de-embossing temperature was too high, as it was still flowing enough to form strings between the mold and imprint when separated. Mold damage was typically a sign that the de-embossing temperature was too low, causing the COC polymer to grip the mold and break off small pieces around the edges of the features. In extreme cases large pieces would break off and rendering the Weicon C mold unusable. Considering these factors 185°C and 173°C were found to be the optimal temperatures for embossing and de-embossing, respectively.

Wafer Bonding Optimization

After embossing, COC wafers were sealed using solvent vapor assisted thermal bonding, a commonly used method that uses pressure to hold solvent activated polymer halves together while heat rapidly drives off the solvent leading to entanglement of polymer chains and the formation of a strong bond.[102] The extent to which each half is activated by the solvent is critically important, as overexposure of the embossed polymer can lead to channel deformation, especially when put under pressure. The low aspect ratio of our μFFE design makes our devices particularly prone to overexposure giving rise to sagging, and potentially bonding in, the separation channel.

When optimizing the exposure time for the imprinted wafer, clarification of the COC polymer was used as a qualitative marker (see Figure 3). Clarification was observable after approximately 12 min of cyclohexane vapor exposure at room temperature. As a result, 12 min was used as the exposure time for the imprinted half to ensure activation while minimizing channel deformation during bonding. However, only 12 min of vapor exposure left the separation channel somewhat opaque. To enhance

clarity, the imprinted wafer was pre-exposed to cyclohexane vapor for 28 min and allowed to dry completely prior to the 12 min exposure for bonding described above.

Tackiness was used, in addition to bonding efficacy and channel deformation, to optimize the exposure time unembossed wafer. Tackiness was characterized by the ability to imprint into and displace the polymer as well as by the two halves sticking together loosely when placed into contact. The polymer halves holding together loosely indicated they were entangling when placed into contact, which occurred after roughly 30 min of cyclohexane vapor exposure. Bonds attempted at this exposure time resulted in incomplete sealing of the device. Overexposure was signified by the ability to imprint into and displace polymer by hand with minimal force, which occurred after approximately 45 min of cyclohexane vapor exposure. Bonds attempted at this exposure time resulted in COC polymer flowing into and distorting the electrode and capillary channels, with the collapse of the separation channel being common. Within this range, 40 min of cyclohexane vapor exposure of the unimprinted wafer was found to produce strong bonds that could not be separated by hand while avoiding collapsing the separation channel. Once sufficiently activated, the imprinted and unimprinted wafers were aligned in a bonding rig and placed in a pre-heated thermal press. Due to the volatility of the solvent the short-lived activated state of the COC polymer, properly aligning the wafers in the bonding rig and placing them in the thermal press under bonding conditions within 1 to 2 minutes was imperative to form a successful bond.

Once the activated wafers were aligned in the thermal press, a load was applied to hold the wafers together while heat was used to drive off the solvent. A 500 lb load was used to hold the COC wafers in firm contact during this step. It was important to keep the temperature high during the bonding step to drive off the solvent quickly and

completely, as residual cyclohexane would form pockets between the bonded wafers, weakening the bond and potentially peeling it apart over time. Typically, a solvent bonding temperature would be chosen slightly below the glass transition temperature of the polymer (i.e. 178°C).[101] However, our use of a 3D printed ABS bonding rig to hold the wafers in place during bonding limited the temperature that we could apply to 93°C.

The bonding rig featured two halves, each with cutouts of the channel design. One half featured a 5.8 cm × 4.5 cm × 0.5 mm indent to help align the wafers in the rig. The other half featured posts at the center of each side that would hold the two halves of the rig in alignment. The bonding rig was key to the process, directing pressure away from the channels thus reducing the likelihood of bonding in the separation channel, while simultaneously helping to hold the two halves in alignment. The use of a 3D printer for production was significant as it allowed the bonding rig to be quickly and cheaply altered to accommodate changes in the master mold design.

Characterization of Embossing Fidelity

Once the optimal fabrication conditions had been determined, imprinted COC wafers were evaluated using a KLA Tencor P-7 surface profiler before and after cyclohexane vapor exposure to assess the effect on the channel dimensions and the fidelity of the structures relative to the CAD file. The effects of sanding the master mold to remove 3D print lines were also determined.

Table 4.1 Comparison between device dimensions predicted from the CAD with those observed in embossed COC wafers before and after 40 minutes cyclohexane vapor exposure.

Feature Depth	CAD (μm)	Pre-exposure (μm)	Post-exposure (μm)
Separation Channel	28	55±6	56±8
Electrode Channels	200	203±2	201±2

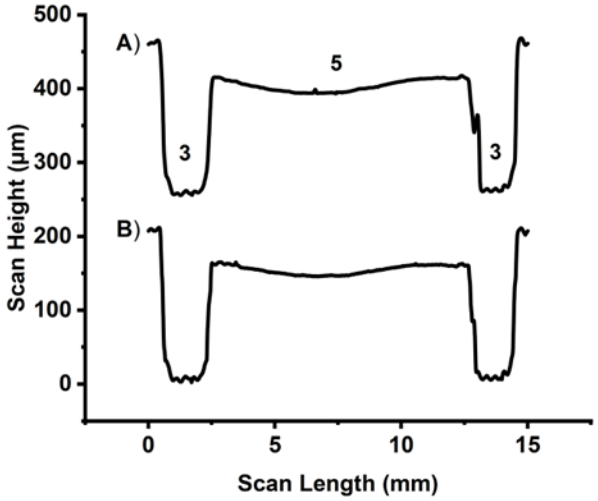

Figure 4.4 KLA Tencor P7 depth profile recorded across the electrode and µFFE separation channels of an embossed COC wafer (A) before and (B) after 40 min cyclohexane vapor exposure at room temperature. (3) and (5) correspond to the electrode and separation channels, respectively as labeled in Figure 4.2.

As shown in Table 4.1 and Figure 4.4, the embossed COC wafer had a significantly deeper separation channel than predicted from the CAD file. This was particularly surprising since a reduced depth was expected due to sanding the master mold. With the electrode channels being consistently the correct dimensions, it is unlikely that the increased depth of the separation channel was the result of systematic printing error or an artifact of the hot embossing process. The added depth in the separation channel is most likely due to a slicing error as the CAD file was processed prior to 3D printing. The deeper than expected separation channel increased its cross-sectional area, which in turn increased the current observed during separations. Increased current is problematic since it limits the maximum separation voltage that can be applied before electrolysis products are generated at a rate faster than they can be cleared from the electrode channels and disrupt stable flow through the device. Additionally, the increased height of the separation channel increases hydrodynamic broadening which scales with the square of the channel height.[2]

A comparison of the electrode and separation channels in Figure 4.4 shows that sanding the master mold minimized 3D printing artifacts in the separation channel of the final embossed COC wafer. Remaining 3D print lines are observable as small, regularly spaced ridges in the in the electrode channels. Sanding successfully removed these ridges from the separation channel. In addition to smoothing the separation channel, sanding introduced a 3-4× increase in the variance in channel height relative to the electrode channels. Sanding also created a distinct valley in the separation channel that affects the flow path of the sample stream, as the stream will follow the deepest portion of the channel. In this geometry the sample stream flows off center to the right of the device, as devices are inverted with respect to Figure 4.4 to avoid inlet and outlet tubing obscuring the separation channel or scattering laser light during detection. While the non-linear flow paths do not have a significant effect on stream width or separation, it does reduce the available separation space for either the negative or positively charged analytes before they forced into the electrode channel depending on electrode polarity. The uneven separation channel could be addressed using profiling to inform further sanding of the master mold to produce a flatter separation channel. Future advances in 3D printer resolution and reduced layer heights may also negate the need for sanding all together.

µFFE Separation and Limits of Detection

Figure 4.5 shows a µFFE separation of three fluorescent dyes with different charges: fluorescein (negative), rhodamine 110 (neutral), and rhodamine 123 (positive) in the COC device. Baseline resolution was achieved at 150V. Fabrication defects can be seen giving rise to minor dead spots where fluorescence is lower than expected in the rhodamine 123 peak of the 150 V scan. We believe this is in part an artifact caused

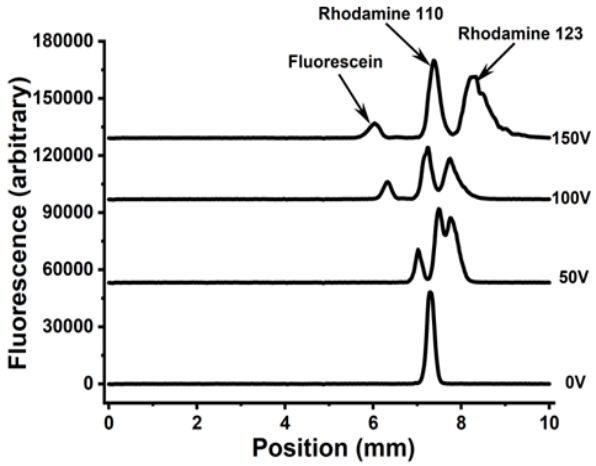

Figure 4.5 µFFE separation of fluorescein (50 nM), rhodamine 110 (500 nM), and rhodamine 123 (2.5 µM) on a hot embossed COC device using LIF detection. The right electrode was held at ground while 0 to +150V was applied to the left electrode.

by solvent evaporation resulting in semi-crystalline regions that can scatter light. Long cyclohexane exposures accentuate the problem, generating the visible groove patterns shown in Figure 4.6. While these dead spots do not impact separation, they could potentially be removed with further optimization of the bonding procedure.

Figure 4.6 An imprinted COC wafer exposed to cyclohexane vapor for approximately 2 h. Excessive cyclohexane vapor exposure gave rise to visibly observable grove patterns in the COC wafer after solvent evaporation.

Loss of sensitivity due to lower optical transparency and surface smoothness is always a concern when transitioning from glass to polymeric substrates as the

fabrication material. To assess the performance of the COC µFFE device, limits of detection (LOD) for the three fluorescent dyes were determined. A stock of the three fluorescent dyes were diluted with separation buffer resulting in five solutions ranging in concentration from 5-500 nM for fluorescein and rhodamine 110, and 50-5000 nM for rhodamine 123. Table 4.2 shows the LOD recorded on the COC device. Observed LODs were comparable with previously reported devices, showing an approximately 3-fold higher LOD than glass devices, and an approximately 2-fold lower LOD than 3D printed ABS devices. This improvement in LOD relative to the 3D printed ABS devices was expected due to the low background fluorescence of COC[73] and the lack of print-lines that are present in the ABS devices.

Table 4.2 Comparison of Limits of Detection between COC, ABS, and glass µFFE devices.

	Fluorescein	**Rhodamine 110**	**Rhodamine 123**
COC Device	2 nM	1 nM	8 nM
Glass Device[6]	0.6 nM	0.3 nM	3 nM
ABS Device[6]	5 nM	2 nM	10 nM

Longevity was a clear advantage of the COC µFFE devices. COC µFFE devices were regularly operated for over a month without failing or showing signs of degradation. This is in stark contrast to ABS µFFE devices which, due to cycles of water adsorption and drying, would become opaque or crack within 2-4 weeks of use.[6] Glass µFFE devices are more robust, operating for approximately 6-12 months before failure of the gold/titanium electrodes. At this early design stage, we regularly cycle out devices before they fail. We anticipate that they will rival and potentially surpass the longevity of glass due to the thicker electrical connections they possess. In addition, COC µFFE devices only cost approximately $50 per unit in non-recoverable materials to produce. While this is significantly more than the approximate $0.20 it costs to produce an ABS device[6], the COC devices remain substantially cheaper than glass devices and don't require a

specialized clean room facility for fabrication. The full design cycle from master mold design to device fabrication can be completed in 6 days. Once the embossing mold is produced, several functional µFFE devices can be fabricated in parallel within a single day.

Conclusion

The current manuscript demonstrates the potential of hot embossing for the high throughput production of low-cost µFFE devices in COC with performance metrics competitive with those previously reported in glass or ABS. Poly-jet 3D printed hot embossing master molds offer the ability to rapidly iterate microfluidic designs and produce high performance devices in desirable materials at low costs. COC µFFE devices could be produced within six to seven days of acquiring a 3D printed master mold. With the continual advancement of 3D printing technology improving resolution, decreasing layer heights, and decreasing costs this technique has the potential for widespread use in the rapid iteration and production of new microfluidic designs. Production could be rapidly scaled up thereafter by fabricating devices in parallel, enabling the production of several µFFE devices in a single day from an embossing mold.

Chapter 5

Summary and Future Direction

Micro free flow electrophoresis (μFFE) is an analytical separation technique that separates analytes in space based on their electrophoretic mobility. As a result of separating in space, μFFE is capable of injecting, separating, and detecting continuously. Due to the continuous nature μFFE separation it is well suited for multidimensional separations, on-line buffer exchange, and continuous monitoring of biological systems. This work focused on optimization of μFFE devices to expand its viability by improving detection sensitivity, tailoring designs for specific applications, and developing cheaper fabrication protocols in high performance materials with the potential for high throughput production.

In Chapter 2 a side-on approach for μFFE laser induced fluorescence (LIF) detection was evaluated as a means of improving sensitivity. In this laser alignment the laser was introduced directly through the side of the device, rather than spreading the laser into a line and reflecting it down onto the surface of the device. Fluorescein samples were streamed through both a glass and 3D printed acrylonitrile butadiene styrene (ABS) device in both side-on and top-down laser alignments with no voltage applied to evaluate the relative impact the alignment change had. For the glass device, a roughly 62% improvement in the limit of detection for fluorescein was observed when using side-on LIF detection without significant optimization of laser power. Theoretically, if this laser alignment were to be applied to the most sensitive μFFE LIF detection method previously recorded[43] a limit of detection for fluorescein of 5.6 pM or lower could be obtained. For the ABS device, however, results were not obtainable for the side-on alignment as the material scattered too much of the laser light to enable safe operation or comparable sensitivity. The failure to function in the 3D printed ABS device showed that this laser alignment is only viable in materials that are highly optically transparent with smooth surfaces and without pockets in the bonded areas. Furthermore, this

alignment requires the device to have a flat smooth edge where the laser is passed into the device which increases the amount of post processing required for a finished device.

Chapter 3 explored the capability of μFFE to perform on-line buffer exchange for the purpose of interfacing incompatible separation techniques. While this application was reported in the early days of μFFE to interface isoelectric focusing (IEF) and electrospray ionization mass spectrometry (ESI-MS)[13], no further developments have been reported. With the further development of μFFE as a separation technique, particularly with regards to efficient interfacing with MS, the application warranted further exploration. Initial designs were developed using computer-aided design (CAD) and 3D printed in ABS, notably featuring a narrow separation channel to enable low voltage removal of the sample buffer from the separation channel into the electrode channel. On-line buffer exchange tests were performed using a sample buffer containing 50 mM sodium phosphate and 300 μM triton X-100 and a running buffer containing 10 mM ammonium acetate and 300 μM triton X-100. Fractions were collected from the anodic electrode channel and separation channel at various voltages and their phosphate concentrations were assessed using a malachite green assay. Significant removal of the phosphate occurred at 75 V, with the amount remaining in the separation channel falling below the limit of detection for the assay. Further increases in voltage resulting in accumulation of electrolysis products in the electrode causing phosphate to be pulled back into the separation channel. The behavior of flow in the device at 125 V was visualized using a sample stream containing 0.5 mM fluorescein, which revealed bubble accumulation and fluid from the electrode channel pulling back into the separation channel.

Comsol Multiphysics modeling was used to assess the flaws of the design and develop a design to resolve its issues as well as foreseeable problems with ESI-MS interfacing. Specifically, improving electrolysis product removal, minimizing the dilution factor of the sample when passing through the device, and the removal of neutral surfactants from the separation channel. Electrolysis product removal was improved by increasing the depth of the electrode channel relative to the separation channel. This resulted in higher linear velocities in the electrode channels that can expel the electrolysis products before they can accumulate and disrupt flow. Minimizing the dilution factor was addressed via designs using additional outlets in the separation channel. While the extent to which this is needed is highly dependent on analyte concentrations. The addition of more outlets to the separation channel also enables the outer outlets to capture sample buffer that may pull back into the separation channel. The removal of neutral surfactants from the separation channel was addressed through the addition of two new inlets to feed surfactant free running buffer into it. Such a design retains the ability to use neutral surfactants in the electrode channels to enable long term flow stability while avoiding the issue of ion suppression these compounds cause with electrospray ionization.

Chapter 4 detailed the development and optimization of a novel fabrication method to produce µFFE devices in cyclic olefin copolymer (COC) via hot embossing. The method opted to use poly-jet 3D printed master molds to enable relatively cheap and easy alterations to the design. Briefly, the poly jet 3D-printed master mold had its separation channel wet sanded using 1500 grit sandpaper to remove the print lines and 3000 grit sandpaper to polish it. The master mold was then cast in silicon, which was subsequently re-cast in Weicon C to produce the embossing mold which was tempered prior to use. An embossing temperature of 185 °C and de-embossing temperature of

173 °C were used with a force of 750 lbs to produce the channel imprints within the COC plaques. Bonding was performed via solvent assisted thermal bonding with 40 and 12 min of room temperature cyclohexane vapor exposure for the fluidic access half and imprinted half of the device, respectively. Once exposed the halves were placed into contact in a bonding rig and placed in a thermal press under 500 lbs of force at 93 °C to cure the bond. Ports were added to the device for fluidic access, the sample capillary was inserted, and the electrode holes were sealed to finish the device. Device profiling was performed to assess the fidelity of the technique which revealed a separation channel approximately twice as tall as designed while the electrode channels were approximately the correct height. The device performance was assessed by performing a three-dye separation with LIF detection, which showed a limit of detection of 2, 1, and 8 nM for fluorescein, rhodamine 110, and rhodamine 123, respectively. Compared to the LODs reported for previous glass and 3D printed ABS devices[6] these results were competitive, being approximately 3-fold higher than glass devices and 2-fold lower than 3D printed ABS device.

Future Direction

The work in this thesis has outlined attempts to make µFFE a more appealing separation method via more sensitive detection, optimizing designs for specific applications, and expanding fabrication methods. Going forward, I believe the future of µFFE research should place emphasis on tailoring and optimizing designs for specific applications where the continuous nature of µFFE separation provides unique benefits like microscale sample purification, multidimensional separations, and continuous monitoring. This is already arguably already the direction the bulk of µFFE research is heading, as shown in the work of Geiger et al.[8,27,28], Johnson et al.[23], Jender et al.[29,30],

Zitzmann et al.[45], and Pfeifer et al.[25] to name a few. However, the variety of possible μFFE designs combined with the generally slow rate of device production leads to an arduous prototyping cycle. Consequently, the slow rate of device prototyping leads to design innovation occurring mainly out of necessity for a desired application, without limited efforts for further optimization.

To improve the rate of design innovation and optimization, I believe a streamlined prototyping workflow should be developed incorporating Multiphysics modeling and multiple fabrication methods, one for rapid prototyping and one for high performance device fabrication. Within this workflow a device would first be modeled to ensure proper function and then produced using a rapid prototyping fabrication method like 3D printing. The device would then be tested to assess the general performance of the design and detect unforeseen problems with the design. Where these problems in the design arise, it can then be quickly altered, modeled, and produced again. Finally, once the design is finalized a high-performance version is produced (i.e. an etched glass μFFE device) and the specific separation conditions can be optimized.

With the speed and low cost of a fabrication method like 3D printing ambitious and perhaps unorthodox designs can be explored and optimized without incurring significant costs. However, the use of 3D printing does come with some tradeoffs. Notably, the print lines created by the 3D printer can alter flow. Though their effects are mitigated through smoothing in the bonding step, it is possible that they may cause unintended effects that are falsely attributed to the device design. Furthermore, the thermoplastics used in 3D printing often contain UV stabilizing dopants to prevent degradation, making them impermeable to UV light. This makes 3D printing ill suited for designs where an ion permeable membrane will be used for electrolysis product mediation, as they would

need to be fabricated separately and introduced to the device in the bonding step. In these cases, liquid lithography between two glass slides can be used. Notably, liquid lithography using glass substrates cannot produce multiple channel heights without glass etching, which would significantly reduce its effectiveness for rapid prototyping. However, the UV transmittance of the substrate makes it well suited for designs incorporating UV polymerized ion permeable membranes, which do not require multiple channel heights.

µFFE is still a relatively new separation technique, but with consistent advances in detection, applications, and fabrication methods it will eventually find more universal adoption in analytical workflows. The side-on LIF detection scheme I introduced demonstrated that there is still significant room for improvement in detection sensitivity. The µFFE designs I presented attempted to optimize the technique for rapid on-line buffer exchange that could allow on-line interfacing between ESI-MS and otherwise incompatible separation techniques. Most significantly, I developed a novel fabrication technique for hot embossing µFFE devices in COC that is capable of relatively quick changes in design. It is my hope that the work I have done will inspire future scientists to make use of the unique capabilities of µFFE, and potentially continue my work optimizing the technique for rapid on-line buffer exchange.

References

1 D. E. Raymond, A. Manz and H. M. Wldmer, *Anal Chem*, 1994, **66**, 2858–2865.

2 B. R. Fonslow and M. T. Bowser, *Anal Chem*, 2006, **78**, 8236–8244.

3 D. Kohlheyer, G. A. J. Besselink, S. Schlautmann and R. B. M. Schasfoort, *Lab Chip*, 2006, **6**, 374–380.

4 B. R. Fonslow and M. T. Bowser, *Anal Chem*, 2005, **77**, 5706–5710.

5 B. R. Fonslow, V. H. Barocas and M. T. Bowser, *Anal Chem*, 2006, **78**, 5369–5374.

6 S. K. Anciaux, M. Geiger and M. T. Bowser, *Anal Chem*, 2016, **88**, 7675–7682.

7 D. E. Raymond, a Manz and H. M. Widmer, *Anal Chem*, 1996, **68**, 2515–2522.

8 M. Geiger, R. K. Harstad and M. T. Bowser, *Anal Chem*, 2015, **87**, 11682–11690.

9 M. Jing and M. T. Bowser, *Lab Chip*, 2011, **11**, 3703–3709.

10 H. Kobayashi, K. Shimamura, T. Akaida, K. Sakano, N. Tajima, J. Funazaki, H. Suzuki and E. Shinohara, in *Journal of Chromatography A*, Elsevier, 2003, vol. 990, pp. 169–178.

11 E. Poehler, C. Herzog, C. Lotter, S. A. Pfeiffer, D. Aigner, T. Mayr and S. Nagl, *Analyst*, 2015, **140**, 7496–7502.

12 Y. Xu, C.-X. Zhang, D. Janasek and A. Manz, *Lab Chip*, 2003, **3**, 224–227.

13 A. Chartogne, U. R. Tjaden and J. van der Greef, *Rapid Communications In Mass Spectrometry*, 2000, **14**, 1269–1274.

14 H. Lu, S. Gaudet, M. A. Schmidt and K. F. Jensen, *Anal Chem*, 2004, **76**, 5705–5712.

15 J. W. Albrecht, J. El-Ali and K. F. Jensen, *Anal Chem*, 2007, **79**, 9364–9371.

16 D. Kohlheyer, J. C. T. Eijkel, S. Schlautmann, A. van den Berg and R. B. M. Schasfoort, *Anal Chem*, 2007, **79**, 8190–8198.

17 Y. A. Song, S. Hsu, A. L. Stevens and J. Han, *Anal Chem*, 2006, **78**, 3528–3536.

18 B. Walowski, W. Hüttner and H. Wackerbarth, *Anal Bioanal Chem*, 2011, **401**, 2465–2471.

19 D. Janasek, M. Schilling, J. Franzke and A. Manz, *Anal Chem*, 2006, **78**, 3815–3819.

20 D. Janasek, M. Schilling, A. Manz and J. Franzke, *Lab Chip*, 2006, **6**, 710–713.

21 M. Becker, C. Budich, V. Deckert and D. Janasek, *Analyst*, 2009, **134**, 38–40.

22 Y. A. Song, M. Chan, C. Cello, S. R. Tannenbaum, J. S. Wishnok and J. Han, *Anal Chem*, 2010, **82**, 2317–2325.

23 A. C. Johnson and M. T. Bowser, *Anal Chem*, 2017, **89**, 1665–1673.

24 S. Jezierski, V. Tehsmer, S. Nagl and D. Belder, *Chemical Communications*, 2013, **49**, 11644–11646.

25 S. A. Pfeiffer, B. M. Rudisch, P. Glaeser, M. Spanka, F. Nitschke, A. A. Robitzki, C. Schneider, S. Nagl and D. Belder, *Anal Bioanal Chem*, 2018, **410**, 853–862.

26 C. Benz, M. Boomhoff, J. Appun, C. Schneider and D. Belder, *Angewandte Chemie - International Edition*, 2015, **54**, 2766–2770.

27 M. Geiger, N. W. Frost and M. T. Bowser, *Anal Chem*, 2014, **86**, 5136–5142.

28 M. Geiger and M. T. Bowser, *Anal Chem*, 2016, **88**, 2177–2187.

29 M. Jender, S. Höving, P. Novo, E. Freier and D. Janasek, *Anal Chem*, 2021, **93**, 7204–7209.

30 M. Jender, P. Novo, D. Maehler, U. Münchberg, D. Janasek and E. Freier, *Anal Chem*, 2020, **92**, 6764–6769.

31 D. Dutta, in *Methods in Molecular Biology*, Humana Press Inc., 2019, vol. 1906, pp. 167–195.

32 D. Dutta, *J Chromatogr A*, 2015, **1404**, 124–130.

33 M. C. Roman and P. R. Brown, *Anal Chem*, 1994, **66**, 86A–94A.

34 N. W. Frost and M. T. Bowser, *Lab Chip*, 2010, **10**, 1231–1236.

35 T. Akagi, R. Kubota, M. Kobayashi and T. Ichiki, *Jpn J Appl Phys*, , DOI:10.7567/JJAP.54.06FN05.

36 S. Jezierski, L. Gitlin, S. Nagl and D. Belder, *Anal Bioanal Chem*, 2011, **401**, 2651–2656.

37 H. Ding, X. Li, X. Lv, J. Xu, X. Sun, Z. Zhang, H. Wang and Y. Deng, *Analyst*, 2012, **137**, 4482–4489.

38 S. Köhler, C. Benz, H. Becker, E. Beckert, V. Beushausen and D. Belder, *RSC Adv*, 2012, **2**, 520–525.

39 C. Herzog, G. F. W. Jochem, P. Glaeser and S. Nagl, *Microchimica Acta*, 2015, **182**, 887–892.

40 D. Kohlheyer, J. C. T. Eijkel, S. Schlautmann, A. van den Berg and R. B. M. Schasfoort, *Anal Chem*, 2008, **80**, 4111–4118.

41 H. Wagner, *Free-flow electrophoresis*, 1989.

42 S. Köhler, S. Nagl, S. Fritzsche and D. Belder, *Lab Chip*, 2012, **12**, 458–463.

43 R. T. Turgeon and M. T. Bowser, *Electrophoresis*, 2009, **30**, 1342–1348.

44 V. Kostal, B. R. Fonslow, E. A. Arriaga and M. T. Bowser, *Anal Chem*, 2009, **81**, 9267–9273.

45 F. D. Zitzmann, H. G. Jahnke, S. A. Pfeiffer, R. Frank, F. Nitschke, L. Mauritz, B. Abel, D. Belder and A. A. Robitzki, *Anal Chem*, 2017, **89**, 13550–13558.

46 R. T. Turgeon, B. R. Fonslow, M. Jing and M. T. Bowser, *Anal Chem*, 2010, **82**, 3636–3641.

47 B. R. Fonslow and M. T. Bowser, *Anal Chem*, 2008, **80**, 3182–3189.

48 A. J. Macgillivray and D. R. Wood, *Eur J Biochem*, 1974, **41**, 181–190.

49 P. H. O'farrells, *High Resolution Two-Dimensional Electrophoresis of Proteins**, 1975, vol. 250.

50 D. R. Deans, *USE OF HEART CUTTING IN GAS CHROMATOGRAPHY A REVIEW*, Elsewer Saentlfic Pubhshrng Company, 1981, vol. 203.

51 V. G. van Mispelaar, A. C. Tas, A. K. Smilde, P. J. Schoenmakers and A. C. van Asten, in *Journal of Chromatography A*, Elsevier, 2003, vol. 1019, pp. 15–29.

52 B. Mitrevski and P. J. Marriott, *Anal Chem*, 2012, **84**, 4837–4843.

53 M. Pursch and S. Buckenmaier, *Anal Chem*, 2015, **87**, 5310–5317.

54 R. Karongo, T. Ikegami, D. R. Stoll and M. Lämmerhofer, *J Chromatogr A*, , DOI:10.1016/j.chroma.2020.461430.

55 M. M. Bushey and J. W. Jorgenson, *Automated Instrumentation for Comprehensive Two-Dimensional High-Performance Liquid Chromatography of Proteins*, Wiley Interscience, 1990, vol. 62.

56 L. W. Potts, D. R. Stoll, X. Li and P. W. Carr, *J Chromatogr A*, 2010, **1217**, 5700–5709.

57 R. E. Murphy, M. R. Schure and J. P. Foley, *Anal Chem*, 1998, **70**, 1585–1594.

58 S. Podszun, P. Vulto, H. Heinz, S. Hakenberg, C. Hermann, T. Hankemeier and G. A. Urban, *Lab Chip*, 2012, **12**, 451–457.

59 T. E. Creighton, S. Hjerten, M. D. J. Zhu, S. Chromatogr ; Hjerten, J. L. Liao, J. J. Yao, F. Chromatogr ; Kilar, M. Yamashita, J. B. Fenn, M. Mann, C. W. Meng, S. F. ; M. G. Wong, A. Blades, T. P. Kebarle, P. Kebarle, L. Tang, R. D. Smith, R. F. Schleif and P. C. Wensink, *Two-Dimensional Analysis of Recombinant E. coli Proteins Using Capillary Isoelectric Focusing Electrospray Ionization Mass Spectrometry*, Springer-Verlag, 1997, vol. 346.

60 Q. Tang, A. Kamel Narrate and C. S. Lee, *Capillary Isoelectric Focusing-Electrospray Mass Spectrometry for Protein Analysis*, IRL Press, 1995, vol. 346.

61 M. H. Lamoree, U. R. Tjaden and J. van der Greef, *Use of microdialysis for the on-line coupling of capillary isoelectric focusing with electrospray mass spectrometry*, 1997, vol. 777.

62 R. K. Mosing, S. D. Mendonsa and M. T. Bowser, *Anal Chem*, 2005, **77**, 6107–6112.

63 S. Saha, S. K. Alamsetti and C. Schneider, *Chemical Communications*, 2015, **51**, 1461–1464.

64 I. German, D. D. Buchanan and R. T. Kennedy, *Anal Chem*, 1998, **70**, 4540–4545.

65 C. X. Zhang and A. Manz, *Anal Chem*, 2003, **75**, 5759–5766.

66 S. Köhler, C. Weilbeer, S. Howitz, H. Becker, V. Beushausen and D. Belder, *Lab Chip*, 2011, **11**, 309–314.

67 C. X. Zhang and A. Manz, *Anal Chem*, 2003, **75**, 5759–5766.

68 A. Gökaltun, Y. B. (Abraham) Kang, M. L. Yarmush, O. B. Usta and A. Asatekin, *Sci Rep*, , DOI:10.1038/s41598-019-43625-5.

69 J. Zhou, A. V. Ellis and N. H. Voelcker, *Electrophoresis*, 2010, **31**, 2–16.

70 A. Mata, A. J. Fleischman and S. Roy, *Biomed Microdevices*, 2005, **7**, 281–293.

71 D. Kohlheyer, J. C. T. Eijkel, S. Schlautmann, A. van den Berg and R. B. M. Schasfoort, *Anal Chem*, 2007, **79**, 8190–8198.

72 W. Zhou, L. Xia, X. Xiao, G. Li and Q. Pu, *Electrophoresis*, 2019, **40**, 2165–2171.

73 C. K. Fredrickson, Z. Xia, C. Das, R. Ferguson, F. T. Tavares and Z. H. Fan, *Journal of Microelectromechanical Systems*, 2006, **15**, 1060–1068.

74 R. K. Jena, C. Y. Yue and Y. C. Lam, *Microsystem Technologies*, 2012, **18**, 159–166.

75 T. B. Stachowiak, D. A. Mair, T. G. Holden, L. J. Lee, F. Svec and J. M. J. Fréchet, *J Sep Sci*, 2007, **30**, 1088–1093.

76 S. Roy, C. Y. Yue, Y. C. Lam, Z. Y. Wang and H. Hu, *Sens Actuators B Chem*, 2010, **150**, 537–549.

77 M. Jing and M. T. Bowser, *Anal Chim Acta*, 2011, **686**, 9–18.

78 N. Pamme and A. Manz, *Anal Chem*, 2004, **76**, 7250–7256.

79 A. Berthold, L. Nicola, P. M. Sarro and M. J. Vellekoop, *Sensors and Actuators*, 2000, **82**, 224–228.

80 C.-H. Wu and H.-C. Kuo, *Journal of Mechanical Science and Technology*, 2007, **21**, 1477–1482.

81 M. Matteucci, T. L. Christiansen, S. Tanzi, P. F. Ostergaard, S. T. Larsen and R. Taboryski, *Microelectron Eng*, 2013, **111**, 294–298.

82 J. Schütte, C. Freudigmann, K. Benz, J. Böttger, R. Gebhardt and M. Stelzle, *Lab Chip*, 2010, **10**, 2551–2558.

83 H. Tachibana, M. Saito, S. Shibuya, K. Tsuji, N. Miyagawa, K. Yamanaka and E. Tamiya, *Biosens Bioelectron*, 2015, **74**, 725–730.

84 B. Y. Pemg, C. W. Wu, Y. K. Shen and Y. Lin, *Polym Adv Technol*, 2010, **21**, 457–466.

85 J. S. Jeon, S. Chung, R. D. Kamm and J. L. Charest, *Biomed Microdevices*, 2011, **13**, 325–333.

86 R. K. Jena, C. Y. Yue, Y. C. Lam and Z. Y. Wang, *Sens Actuators B Chem*, 2010, **150**, 692–699.

87 A. D. Castiaux, C. W. Pinger, E. A. Hayter, M. E. Bunn, R. S. Martin and D. M. Spence, *Anal Chem*, 2019, **91**, 6910–6917.

88 A. D. Castiaux, E. R. Currens and R. S. Martin, *Analyst*, 2020, **145**, 3274–3282.

89 V. Bertana, C. Potrich, G. Scordo, L. Scaltrito, S. Ferrero, A. Lamberti, F. Perrucci, C. F. Pirri, C. Pederzolli, M. Cocuzza and S. L. Marasso, *Journal of Vacuum Science & Technology B, Nanotechnology and Microelectronics: Materials, Processing, Measurement, and Phenomena*, 2018, **36**, 01A106.

90 K. Piironen, M. Haapala, V. Talman, P. Järvinen and T. Sikanen, *Lab Chip*, 2020, **20**, 2372–2382.

91 B. M. Brenda, S. Griveau, F. Bedioui, F. d' Orlye, J. A. F. da Silva and A. Varenne, *Electrochim Acta*, , DOI:10.1016/j.electacta.2022.139888.

92 M. D. Nelson, N. Ramkumar and B. K. Gale, *Journal of Micromechanics and Microengineering*, , DOI:10.1088/1361-6439/ab2f26.

93 G. Gaal, M. Mendes, T. P. de Almeida, M. H. O. Piazzetta, Â. L. Gobbi, A. Riul and V. Rodrigues, *Sens Actuators B Chem*, 2017, **242**, 35–40.

94 F. Li, N. P. Macdonald, R. M. Guijt and M. C. Breadmore, *Anal Chem*, 2017, **89**, 12805–12811.

95 F. Kotz, M. Mader, N. Dellen, P. Risch, A. Kick, D. Helmer and B. E. Rapp, *Micromachines (Basel)*, , DOI:10.3390/mi11090873.

96 F. M. Mwema and E. T. Akinlabi, in *SpringerBriefs in Applied Sciences and Technology*, Springer, 2020, pp. 1–15.

97 N. Shahrubudin, T. C. Lee and R. Ramlan, in *Procedia Manufacturing*, Elsevier B.V., 2019, vol. 35, pp. 1286–1296.

98 O. Gülcan, K. Günaydın and A. Tamer, *Polymers (Basel)*, 2021, 13.

99 K. Giri and C. W. Tsao, *Micromachines (Basel)*, 2022, 13.

100 C. W. Tsao and D. L. DeVoe, *Microfluid Nanofluidics*, 2009, 6, 1–16.

101 Q. Li, B. Jiang, X. Li and M. Zhou, *Micromachines (Basel)*, 2022, **13**, 965.

102 T. Guan, S. Yuket, H. Cong, D. W. Carton and N. Zhang, *ACS Omega*, 2022, **7**, 20104–20117.

103 A. J. Berger, Y. Wang and M. S. Feld, *Appl Opt*, 1996, **35**, 209–212.

104 E. Haustein and P. Schwille, *Curr Opin Struct Biol*, 2004, 14, 531–540.

105 J. R. Auclair, *Trends Biotechnol*, 2019, 37, 5–9.

106 D. Nebija, C. R. Noe, E. Urban and B. Lachmann, *Int J Mol Sci*, 2014, **15**, 6399–411.

107 C. L. Gaughan, *Mol Divers*, 2016, 20, 255–270.

108 H. Zhang, W. Cui and M. L. Gross, *FEBS Lett*, 2014, 588, 308–317.

109 K. Brorson and A. Y. Jia, *Curr Opin Biotechnol*, 2014, 30, 140–146.

110 X. Li, N. A. Pierson, X. Hua, B. A. Patel, M. H. Olma, C. A. Strulson, S. Letarte and D. D. Richardson, *J Pharm Sci*, , DOI:10.1016/j.xphs.2022.10.018.

111 P. Batys, M. Nattich-Rak and Z. Adamczyk, *Physical Chemistry Chemical Physics*, 2020, **22**, 26764–26775.

112 V. Pacáková and K. Štulík, *Encyclopedia of Analytical Science*, 2005, 354–361.

113 K. Itaya and M. Ui, *Clin. Chim. Acta*, 1966, **14**, 361–366.

114 Y. Ishihama, H. Katayama and N. Asakawa, *Anal Biochem*, 2000, **287**, 45–54.

115 R. M. Weinheimer, D. Fennell Evans and E. L. Cussler, *Diffusion in Surfactant Solutions*, 1981.

116 H. Takehara, S. Sato and T. Ichiki, *Applied Physics Express*, , DOI:10.7567/1882-0786/ab3d64.

117 M. Jender, P. Novo, D. Maehler, U. Münchberg, D. Janasek and E. Freier, *Anal Chem*, 2020, **92**, 6764–6769.

118 J. Zhang, C. Das and H. Z. Fan, *Microfluid Nanofluidics*, 2008, **5**, 327–335.

119 J. Forsyth, J. M. Pereña, R. Benavente, E. Pérez, I. Tritto, L. Boggioni and H. H. Brintzinger, *Macromol Chem Phys*, 2001, **202**, 614–620.

120 M. Matschuk, H. Bruus and N. B. Larsen, *Microelectron Eng*, 2010, **87**, 1379–1382.

121 J. Karttunen, J. Kiihamaki and S. Franssila, *Micromachining and Microfabrication Process Technology VI*, 2000, **4174**, 90–97.

122 J. D. Kechagias, V. Iakovakis, P. Stavropoulus, E. Giorgo, A. Koutsomichalis and N. Vaxevanidis, in *Poly Jet 3D Printing Optimization*, 2014, pp. 2877–2888.

123 C. Khan Malek, J. R. Coudevylle, J. C. Jeannot and R. Duffait, *Microsystem Technologies*, 2007, **13**, 475–481.

124 H. Becker and U. Heim, *Sensors and Actuators*, 2000, **83**, 130–135.